Chemical Geology 498 (2018) 17–30

Contents lists available at ScienceDirect

Chemical Geology

journal homepage: www.elsevier.com/locate/chemgeo

From unweathered core to regolith in a single weathering andesitic clast: Rates and trends of in situ chemical weathering on a tropical volcanic island (Basse Terre Island, French Guadeloupe)

Peter B. Sak[a,b,*], Mariah Murphy[c], Lin Ma[d], Jerome Gaillardet[e,f], Elizabeth M. Herndon[g], Susan L. Brantley[b], Christopher Daniel[h]

[a] Department of Earth Sciences, Dickinson College, Carlisle, PA, USA
[b] Earth and Environmental Systems Institute and Dept. of Geosciences, Pennsylvania State University, University Park, PA, USA
[c] Department of Chemistry, Dickinson College, Carlisle, PA, USA
[d] Department of Geological Sciences, University of Texas at El Paso, TX, USA
[e] Institut de Physique du Globe de Paris, Sorbonne Paris Cité, Univ. Paris Diderot, CNRS, Paris, France
[f] Institut Universitaire de France, Sorbonne Paris Cité, Univ. Paris Diderot, CNRS, Paris, France
[g] Department of Geology, Kent State University, Kent, OH, USA
[h] Department of Geology, Bucknell University, Lewisburg, PA, USA

ARTICLE INFO

Editor: Michael E. B

Keywords:
Chemical weathering
Critical Zone
Weathering rinds
Redox
French Guadeloupe

ABSTRACT

We conduct X-ray microprobe, chemical and U-series isotope analyses on an oriented weathering clast collected from the regolith of a weathered Quaternary volcanoclastic debris flow on Basse Terre Island, French Guadeloupe. The sample consists of an unweathered basaltic andesite core surrounded by a weathering rind, and an indurated crust that separates the rind from the overlying soil matrix. U/Th disequilibria dating indicates that rind age increases away from the core-rind boundary to a maximum of 66 ka. This translates to a rind-advance rate of ~0.2 mm kyr^{-1}, broadly consistent with rind advance rates calculated elsewhere on Basse Terre Island. The overlying indurated crust is 72 ka, indicating a possible minimum duration of the rind formation. Elemental variations are constrained by a bulk chemical analysis along a vertical transects from the core to the overlying soil matrix and parallel electron microprobe analyses. The hierarchy of elemental loss across the core-rind boundary varies in the order Ca > Na ≈ Mg > K > Mn > Si > Al > Ti = 0 > P > Fe, consistent with the relative loss of phases in the clast from plagioclase ≈ glass ≈ pyroxene > apatite > ilmenite. The abrupt, < 900 μm wide, Ca, Na and porosity reaction fronts at the core-rind boundary approximately equal the length of the long dimension of plagioclase phenocrysts observed in the unweathered core. The < 1000 μm wide reaction front at the rind-soil interface is marked by an indurated horizon with Fe and Mn enrichment that spans into enrichment of Mn, Ba, Al, Mg and K in the soil matrix. Unlike previously studied clasts, the preservation of the rind-soil interface permits characterization of weathering reactions and material exchanges between the weathering core, the rind, and the surrounding soil matrix, shedding insights into communication between the enveloping weathering rind and host regolith. The lack of an enrichment signal of Mn within the weathered rind suggests that weathering processes active within clasts are distinct from surrounding soil formation processes.

1. Introduction

The chemical weathering of silicate rocks exerts a first-order control on the global carbon cycle (Walker et al., 1981), cycling of nutrients in terrestrial ecosystems (Chadwick et al., 1999), and shaping of landscapes by producing erodible materials (Anderson et al., 2002; Hilton et al., 2011). Commonly, a weathering and eroding profile consists of fresh, unweathered bedrock, overlain by weathered regolith. This fragile skin is a crucial part of the Earth surface layer, commonly referred to as the Critical Zone that extends from the outermost extent of vegetation to the lower limits of groundwater (Brantley et al., 2007a). At depth, water permeates into the bedrock, facilitated by mechanical fracturing and the formation of secondary porosity (White et al., 1998; Calmels et al., 2011). As this reactive fluid migrates through the material, the reaction front between unaltered and altered material migrates downward, causing the lower boundary of the Critical Zone to

* Corresponding author at: Department of Earth Sciences, Dickinson College, Carlisle, PA, USA
E-mail address: sakp@dickinson.edu (P.B. Sak).

https://doi.org/10.1016/j.chemgeo.2018.08.015
Received 27 March 2018; Received in revised form 13 August 2018; Accepted 15 August 2018
Available online 19 August 2018

advance into the bedrock (Brantley et al., 2007b).

Although this deep weathering front can be imaged with geophysical techniques (Braun et al., 2009; Holbrook et al., 2014; Parsekian et al., 2015) or drilled (e.g., White et al., 2001; Anderson et al., 2002; Brantley et al., 2013), it is commonly inaccessible for in situ sampling and detailed characterization. Within the regolith pile, processes such as the mechanical fracturing of bedrock produce rock fragments, referred to here as clasts, which migrate upward through the Critical Zone from the perspective of a land surface experiencing physical denudation. Other processes such as pyroclastic flows may also add rock fragments into regolith profiles to form clasts. As a clast migrates through the Critical Zone, it is chemically altered, resulting in the conversion of unweathered parent material into a discolored and permeable weathering rind, commonly enriched in immobile oxides (i.e., Fe_2O_3, TiO_2, Al_2O_3) relative to the enveloped unweathered core (Colman, 1982a, 1982b). As the duration of weathering increases, the thickness of the weathering rind increases (i.e., Cernohouz and Solc, 1966; Colman and Pierce, 1981; Chinn, 1981; Knuepfer, 1988; Whitehouse et al., 1986; Oguchi, 2004; Sak et al., 2004; Kirkbride, 2005; Pelt et al., 2008) and angular corners of the core-rind boundary become progressively more blunted (Kirkbride and Bell, 2010; Sak et al., 2010; Ma et al., 2012; Lebedeva et al., 2015). Previous studies have demonstrated that the chemical conversion of core to rind material is both in situ and isovolumetric (Sak et al., 2004, 2010). In previous studies of weathering rinds developed in temperate climates on clasts within glacial moraine deposits (Colman and Pierce, 1981), glacial striations were recognized on the outer surface of the weathering rind. From this observation, we infer that rind formation is the chemical weathering end member of field weathering in the absence of physical erosion and analyzing the core-rind boundary of clast samples provides valuable means to study the initiation and duration of chemical weathering at a deep weathering front.

When clasts have been removed from exposures in the field previously, the rind disaggregated such that a fraction of the weathering rind and the rind-matrix boundary remained in the exposure (e.g., Sak et al., 2010; Navarre-Sitchler et al., 2011). As a result, previous studies of clasts are limited to the core-rind boundary, where chemical weathering begins, and did not investigate the outer boundary between the weathering rinds and the surrounding soil matrix material. In this study, we focus on one particular sample that spans from the unweathered core material across the weathering rind and into the surrounding soil matrix material, as evidenced by the presence of an indurated crust.

This approach is also used as an analog for alteration that occurs throughout the critical zone, and can be used to characterize chemical alteration between the bedrock, weathering rind (saprolite), and regolith on a smaller scale without the complications associated with landscape position (Drever and Zobrist, 1992), duration of weathering (Maher et al., 2004), regional variations in parent material (Bluth and Kump, 1994; Louvat and Allegre, 1997), texture (Stefansson and Gislason, 2001), composition (Gislason and Eugster, 1987), physical weathering (Millot et al., 2002; Anderson et al., 2002; West et al., 2005; Emberson et al., 2016), or changes in microclimate (Meybeck, 1987; Raymond, 2017) that confound soil profile and catchment scale investigations.

Here field observations are combined with optical and scanning electron microscope observations spanning from the unweathered core, across the weathering rind and into the overlying soil matrix. Physical and chemical observations as well as major element and U-series isotope analysis of the core, rind, crust and soil matrix are used to fully characterize the weathering system and communication among the various components. These analyses allow for the first in-depth integrated field and laboratory analysis to understand the formation of an entire weathering clast system. Detailed characterizations of transformations associated with the core-rind boundary are used to demonstrate that this clast is similar to previously studied clasts (e.g., Sak et al., 2004, 2010; Ma et al., 2012; Engel et al., 2016). Additionally, the U-series disequilibria measured across the rind of this clast enable us to constrain the weathering rind advance rate. These data add an additional point to the current regional compilation comparing independently constrained catchment scale chemical weathering rates (Gaillardet et al., 2011) to clast-scale weathering rates for clasts within those catchments on the island of Basse-Terre (Ma et al., 2012; Engel et al., 2016). While the previous clast studies have viewed chemical weathering as facilitated only by dissolution from the core to the rind, we present new evidence from X-ray microprobe analyses (micro-X-ray fluorescence mapping [μXRF] and micro-X-ray absorption near edge structure spectroscopy [μXANES]) that fluctuating redox conditions in regolith above the clast results in elemental leaching from the soil matrix and accumulation of oxides at the rind-matrix reaction front.

2. Geologic setting

Basse-Terre Island in the Guadeloupe archipelago of the Lesser Antilles arc is a small (~850 km^2) volcanic island (Fig. 1a and b). Bedrock age decreases linearly from north to south parallel to the topographic divide (Samper et al., 2007, Fig. 1c). Volcanic flows in the immediate vicinity of the study area are $^{40}Ar/^{39}Ar$ dated around 620 ka (Samper et al., 2007), indicating that the duration of weathering of the clast must be ≤620 ka. The pronounced precipitation gradient and straightforward north-south age progression have made Basse-Terre a suitable location to investigate the influence of mean annual precipitation (MAP) on chemical weathering rates at the clast (Engel et al., 2016) and watershed scales (Gaillardet et al., 2011; Dessert et al., 2015). The MAP, as constrained by the NASA Tropical Rainfall Measurement Mission (TRMM, Huffman et al., 2007) varies from 200 to > 6500 mm/a along an east-west oriented gradient meaning that areas of similar bedrock age, but differing MAP, can be compared (Fig. 1b).

The sample was collected from a deposit exposed to a warm (MAT = 25 °C) and wet (MAP = ~4500 mm/a, TRMM data; trmm.nasa.gov) climate (Fig. 1b). The sampled road cut into volcaniclastic debris flows and ash deposits in the Lezarde watershed exposes a well-developed (2–15 m thick) weathering profile (Fig. 2a). Within the steep exposure of the road cut, two debris flows were distinguished in the field by color, texture, and abundance of weathered rock fragments. The lower debris flow is a clayey loam unit that is ≥1.5 m thick, with well-rounded volcaniclastic clasts of variable size and composition that comprise > 30% of the exposed road cut area. The weathered clasts in the lower debris flow are comprised of unweathered andesitic cores enveloped by porous rind material deposited within a dark yellowish-red soil matrix (Munsell Color Notation 5YR). The upper boundary of the lower debris flow is marked by an abrupt (2 cm thick) black (Munsell Color Notation 5Y) horizon. This low relief surface is ornamented with discontinuous black films (most likely enriched in Mn oxides) that extend laterally, and a non-planar boundary overlain by a ~1 m thick reddish yellow (Munsell Color Notation 7.5 YR) ash deposit that is devoid of clasts. In turn, the weathered ash unit is overlain by a brown (Munsell Color Notation 7.5 YR) debris flow. This upper debris flow is differentiated from the lower debris flow by smaller sized clasts that are subangular, an absence of unweathered cores and extensive alteration. Both of the debris deposits become progressively more weathered upsection.

3. Methods

3.1. Field sampling

The sampled clast (Fig. 2b) was collected from the B horizon of the lower debris flow, 1.1 m below the base of the ash deposit. In the field, weathered clasts are readily distinguished from the matrix by textural and color variations. The weathering rind material is brownish yellow

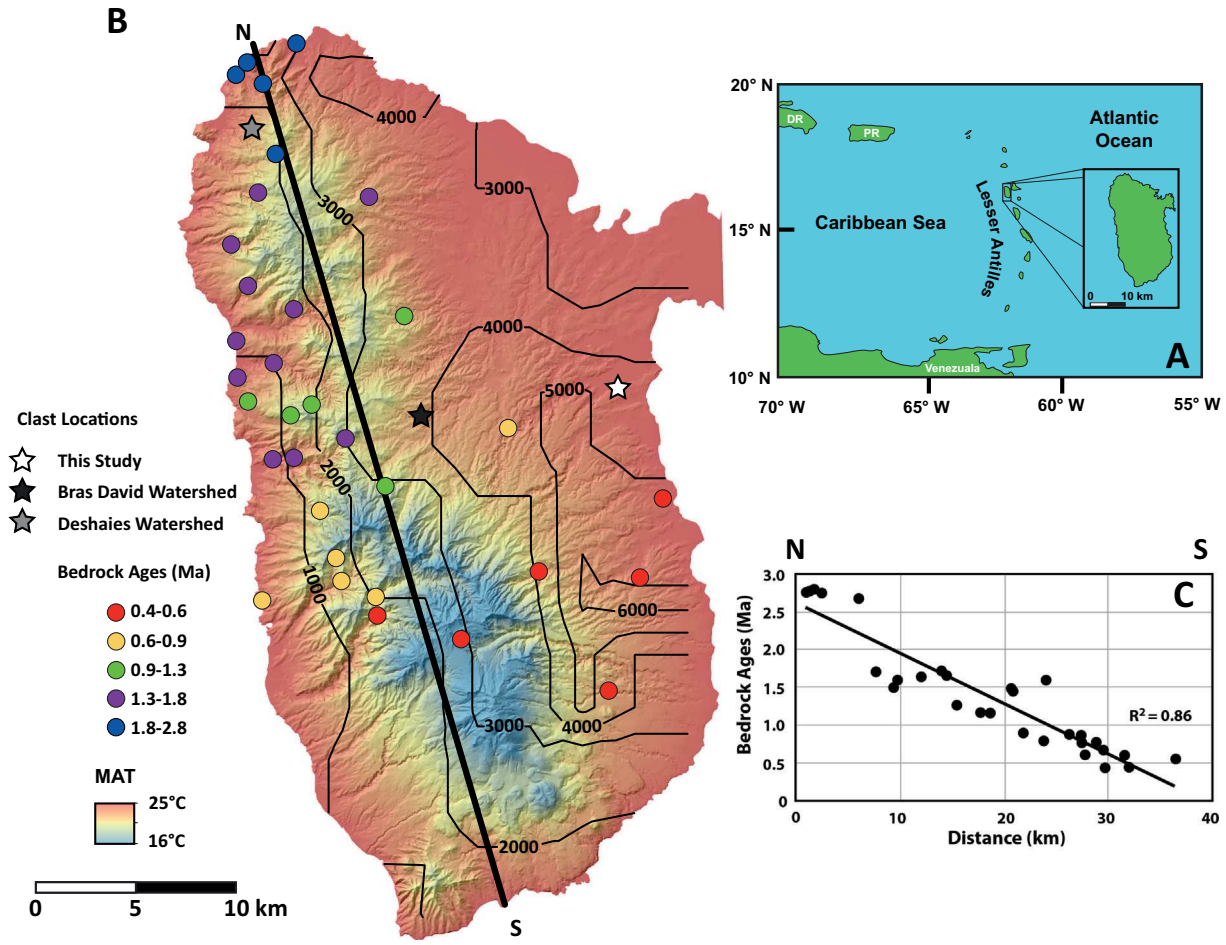

Fig. 1. A) Location map of the Lesser Antilles Arc showing the location of Basse-Terre Island. B) Digital Elevation model of Basse-Terre Island color coded for mean annual temperature (MAT), contoured for TRMM-derived mean annual precipitation (MAP) in mm yr^{-1} (from Huffman et al., 2007), Ar/Ar ages of bedrock (from Samper et al., 2007) shown as small circles; heavy black line shows the transect for C. C) Plot of bedrock age as a function of distance from the northern end of Basse-Terre island. Individual samples are projected onto the heavy black line shown in B.

(Munsell Color Notation 10YR), and the soil matrix material is a dark yellowish red (Munsell Color Notation 5YR). Before the clast was removed from the exposure, the orientation of the vertical axis was marked on the clast. Then the clast was carefully removed from the outcrop, preserving the friable rind and matrix material overlying the unweathered core, and immediately wrapped in aluminum foil and masking tape in the field to preserve the structure of the overlying rind and matrix material. Orientation information was then marked on the exterior of the wrapped clast.

As the sampled clast was extracted from the exposure, weathered rind material from the underside of the clast detached from the core and remained in the exposure. Samples of this disaggregated rind material and the surrounding matrix were mixed with deionized water to create a slurry used to measure field pH conditions.

3.2. Clast sectioning and characterization

In the laboratory, slits were cut into the wrapping around the clast and the sample was immersed in molten paraffin wax for 30 min, so that the wax could permeate throughout the porous material and preserve the structure of the friable rind and matrix material. The immersed clast was allowed to solidify completely for 4 h. The encasing wax was then melted in a desiccation oven at 60°C for 4 h. The wax within the clast was then left at room temperature to solidify. The clast was then cut parallel to the vertical axis using a rock saw, and scanned on a desktop scanner at a resolution of 1200 dpi (1 pixel = 8×10^{-3} mm^2). The thickness of the core, rind, and matrix sections were measured five times along transects oriented perpendicular to the boundaries and spaced 1 cm apart using a digital caliper, and averaged.

3.3. Textural and mineralogical analysis

A single oriented thin section billet was cut from the low curvature top portion of the clast (Fig. 2b) and vacuum impregnated with blue epoxy to highlight the presence of macroscopic porosity. Optical microscopy (OM) of the thin section was used to establish the modal abundance of phases in the core by point counting spots in 1 mm × 1 mm increments at 100× magnification (n = 119). This was paired with the textural and mineralogical analysis from an optical and environmental scanning electron microscope (ESEM; FEI Quanta 400).

Bulk mineralogy in the core and rind was determined by X-ray diffraction (XRD) using a Panalytical X'Pert Pro MPD X-ray diffractometer operating at 40 kV and 45 mA with a Dmax-B controller and CuKα radiation. Whole rock samples were prepared for XRD by grinding rind material disengaged from the core and separate samples of core material. Oriented clay mounts of the rind material were prepared by suspending rind material in a 1% sodium pyrophosphate solution (to prevent flocculation) and sonicating for 1 h. The solution then was allowed to sit for 4 h. Oriented clay mounts were prepared by extracting the < 2 μm fraction that remained in suspension with a pipet, and dropping some of the liquid faction onto a glass slide. The glass

slide was placed in a desiccator until dried. Clay separates were analyzed from 2.5° to 25° 2θ with a 0.01° step size. Whole rock samples of rind, crust and matrix material were analyzed from 3° to 45° 2θ with a 0.01° step size.

Bulk porosity at the mm scale was estimated using image analysis of a high-resolution photomosaic of the entire thin section. The photomosaic was created by stitching together 285 individual photomicrographics taken at 5× magnification (Fig. 2b). The photomosaic was then analyzed using an image processing script in Matlab that isolated the RGB color spectra range corresponding to the blue epoxy. The porosity profile represents the sum total number of blue epoxy pixels in each column of the photomosaic. Porosity is plotted as a function of distance measured perpendicular to the core-rind boundary. The rind-crust and crust-matrix boundaries parallel the core-rind boundary (Fig. 2b).

3.4. Chemical analysis

Variations in bulk elemental compositions across the weathering clast system were determined through chemical analysis. Two parallel transects spanning the sample from core to overlying matrix material were analyzed. Samples of the core, rind, crust and matrix materials were collected as powders using a 3.2 mm diameter carbide-tipped bit to a depth of 5 to 15 mm for seven locations along the linear transect (Fig. 2b). Each sample location was defined by its distance away from the visually defined core-rind boundary. Distance was noted as increasing towards the matrix.

These samples, as well as the samples of the volcaniclastic debris flow matrix, were digested using Li metaborate fusion (Suhr and Ingamells, 1966; Ingamells, 1970; Feldman, 1983) and analyzed for Ti, Si, Al, Ca, Mg, Na, K, Fe, Mn, and P using a Perkin-Elmer 5300DV inductively coupled plasma-atomic emission spectrometer (ICP-AES) in the Pennsylvania State University (PSU) Materials Characterization Laboratory. The samples were analyzed along with several USGS standards including Columbia River (BCR-1) and Hawaiian Volcano Observatory (bhvo-1) basalts. The standards were used to define calibration curves that were in turn used to determine sample compositions. Based on long-term comparisons, the analytical precision is estimated to equal 2–5% for the ICP-AES analyses, except for P in very low concentrations where reproducibility is generally lower.

Chemical variations were further constrained at a higher spatial resolution by analyzing the polished thin section using a Cameca SXFive electron microprobe (EMP) at the PSU Materials Characterization Lab. The EMP was standardized with mineral and glass standards from the PSU collection. Standards included Amelia albite, Hunt olivine, NASA basalt (synthetic lunar basalt glass), and a synthetic diopside glass standard distributed by the Smithsonian Institution (Wash. D.C., U.S.A.). Instrumental parameters were identical in calibration and measurement of unknowns. Based on long-term comparisons, the analytical precision is estimated to be < 1% for the EMP analyses. Correction procedures used "ϕ-ρ-Z" models for ZAF correction factors (Pouchou and Pichou, 1987).

EMP analyses were completed at points across the entire thin section. Points were spaced at 100 μm increments, with a spot size of 50 μm diameter and ~1 μm depth. K, Na, Ca, Fe, Ti, Mg, Si, P, Al, Mn, and Ba were measured at all points. Points measured at the same distance from the core-rind boundary were used to define an average value for that position. This averaging was performed because the spot size was often smaller than the crystal size; therefore, averaging allowed averaged rock analyses rather than individual grain analyses. To determine averages, the profiles were aligned as a function of distance relative to the visually defined core-rind boundary. The core-rind boundary was assigned a value of 0 μm, where distance increased across the rind towards the matrix and negative values correspond to samples coreward of the core-rind boundary.

One backscatter electron (BSE) image and several net intensity maps

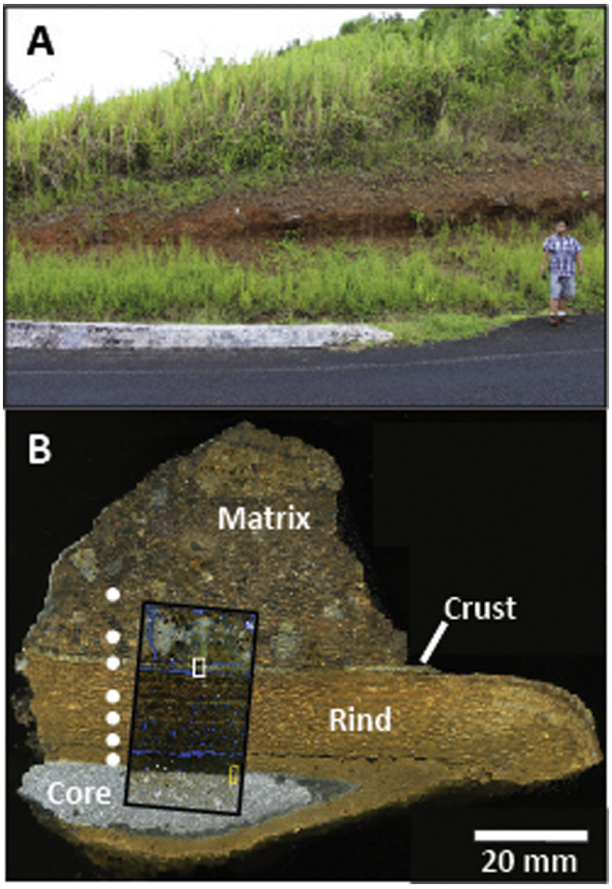

Fig. 2. A) Field photograph of the sampled road cut. B) Oriented photograph of cut section of the analyzed clast showing the core, rind crust and matrix. Thicknesses were measured normal to the visually defined core-rind boundary. Black box shows the extent of the thin-section. Within the thin section, blue shows the extent of epoxy, the yellow box delineates the extent of Fig. 4, and white box delineates the extent of Fig. 8. (For interpretation of the references to color in this figure legend, the reader is referred to the web version of this article.)

of the core-rind and rind-crust-regolith boundaries were produced with a FEI Quanta 400 ESEM and an EDAX Octane Plus EDS system (Department of Geology, Bucknell University). Net intensity maps for the elements Si, Al, P, Fe, Mg, Mn, Ti, Ca, Na, and K were constructed using live spectral mapping. Between 128 and 150 frames were collected across the area of interest with an accelerating voltage of 15 kV and dwell time of 200 to 500 μS. Beam spot size was adjusted to maintain a deadtime of 15%–25% and a count rate of approximately 20,000 cps to 50,000 cps. Spatial resolutions for the maps is between ~3 μm × 3 μm and 5 μm × 5 μm per pixel. The compositional profiles or line scans reported for Na, Ca, Fe, Al, and Si are oriented perpendicular to the core-rind boundary and each point represents an integrated value across the column of pixels oriented perpendicular to the line traverse.

3.5. U-series isotope analysis

U and Th concentrations and isotopic ratios were determined using 20–100 mg of powdered samples from the core, rind, crust and matrix, each of which were spiked with artificial ^{233}U-^{229}Th tracer before sample digestion at the University of Texas at El Paso (UTEP). The samples were completely dissolved with HNO_3-HF and HCl-H_3BO_3 in a two-step procedure. The U and Th were then separated and purified using conventional ion exchange chromatography (see Pelt et al., 2008; Ma et al., 2012) in a clean room facility at UTEP. Isotope ratios of

$^{234}U/^{238}U$ and $^{233}U/^{238}U$ were analyzed using ~50 ng U per sample on a Nu-plasma multiple collector inductively coupled plasma mass spectrometer (MC-ICP-MS) at UTEP. The standard sample bracketing technique was used to correct for drafting of ion counter gains and mass discrimination during measurements (NBL 145B as U bracketing solution). Activity ratios of ($^{234}U/^{238}U$) and U concentrations were calculated from measured $^{234}U/^{238}U$ and $^{233}U/^{238}U$ isotope ratios and the uncertainties of ($^{234}U/^{238}U$) and U concentrations were ~0.5%. USGS rock reference standard (BCR-2) was analyzed along with samples as a QA. Measured values for BCR-2 are: ($^{234}U/^{238}U$) = 1.002 ± 0.003 and U concentration = 1.678 ± 0.025 ppm (n = 2); both are consistent with reference values: BCR-2 ($^{234}U/^{238}U$) = 1.000 and U concentration = 1.69 ± 0.02 ppm (Sims et al., 2008). Procedural blanks for U were ~30 pg and negligible.

3.6. Synchrotron-source X-ray microprobe analysis

X-ray microprobe analyses (micro-X-ray fluorescence mapping [μXRF] and micro-X-ray absorption near edge structure spectroscopy [μXANES]) on the polished thin section were conducted at beamline 13-ID-E (GeoSoilEnviroCARS) at the Advanced Photon Source (APS) at Argonne National Laboratory in March 2015. Beamline 13-ID-E utilizes an undulator-source with a photon flux of ~6×10^{11} s^{-1} for the focused (2 × 2 μm) beam. Hardware included Kirkpatrick-Baez mirrors to focus the beam and a Vortex ME4 silicon drift diode array fluorescence detector. Micro-XRF maps (400 × 400 μm) were measured for six regions across the thin section, including the core (n = 1), rind (n = 2), crust (n = 2), and matrix (n = 1), at an incident energy of 7100 eV with a 3 μm step size and 30 ms/pixel dwell time. The incident energy was selected to reduce Fe fluorescence to help isolate the Mn Kα peak; however, Fe fluorescence intensities could not be resolved in region Crust-2 because exceptionally high Mn fluorescence resulted in large Mn Kβ and scattering peaks that obscured the Fe Kα and Kβ peaks. Fe distribution maps were constructed using the Fe Kα fluorescence peak for the remaining regions (Core, Rind-2, Crust-1, Matrix), with Mn Kβ and Fe Kα overlap occurring only in few discrete Mn-rich spots in the Crust-1 and Matrix maps. XRF maps were generated in MapViewer v.8 (Larch v.0.9.24; Newville, 2013) to depict qualitative differences in fluorescence counts for each element within each map.

Fluorescence-yield Mn K-edge and Fe K-edge μXANES spectra were collected from points of interest identified in the μXRF maps and processed with Athena software (v 0.9.20; Larch version 0.9.24). Data were pre-edge subtracted and post-edge normalized. Edge energies (E_0) for all spectra were defined by the first peak in the μ(E) derivative spectrum following the pre-edge peak. Energy calibration was not required because the Fe K-edge recorded for a zero-valent Fe foil during the sample run (E_0 = 7110.70 eV) was within 0.1 eV of the reference Fe foil (E_0 = 7110.75 eV). Linear combination fits (LCFs) were performed from −20 to +30 eV around the K-edge to determine the average oxidation state of Mn and Fe at each point of interest. Fe spectra were not evaluated for a subset of points (n = 21) where Fe fluorescence saturated the detector. Sample spectra were fit with single-valent reference compounds, and the oxidation state was calculated as the sum of the fractions of individual components. Reference Fe K-edge spectra ($Fe^{II}O$, siderite, pyrite, $FeSO_4$, $FeCl_3$, goethite, hematite, akaganeite, and 2-line ferrihydrite) were obtained from a library of reference compounds recorded at beamline 10.3.2 at the Advanced Light Source. Reference Mn K-edge spectra (n = 17) were reported by Manceau and Nagy (2012). All reference spectra were energy calibrated to E_0 = 6537.7 eV for Mn and E_0 = 7110.75 eV for Fe (following Kraft et al., 1996) as determined by the inflection point of the first-derivative of Mn and Fe metallic foils.

4. Results

4.1. Clast sectioning and characterization

The wrapped sample measured approximately 15 cm in diameter. When the sample was cut in half parallel to the vertical axis, four distinct layers separated by parallel, abrupt planar boundaries were revealed. From bottom to top, the four layers are: i) a 11.7 ± 3.2 mm section of core, ii) a 19.0 ± 0.2 mm thick section of rind, iii) a 1.9 ± 0.2 mm thick crust, and iv) > 28.7 mm of overlying matrix (regolith) material (Fig. 2b). The gray basaltic andesite core is easily distinguished from the surrounding yellowish brown weathering rind. The core-rind boundary is marked by an abrupt transition. The boundary between the weathered rind and surrounding soil matrix is marked by a narrow (~2 mm thick), dark gray, indurated crust bracketed by parallel < 200 μm thick fractures that are filled with epoxy (Fig. 2b). The crust is presumed to either represent the initial boundary between the unweathered clast and the surrounding matrix material or a precipitate layer at the core-soil matrix boundary prior to rind development. Either way, as weathering proceeded, we infer that the core-rind boundary migrated core-ward through time, consuming core and increasing rind thickness. The surrounding soil matrix is distinguished from the weathering rind and crust by a lower pH (4.1 compared to 4.4 in the weathering rind) and the heterogeneous texture and color (Fig. 2b).

4.2. Textural and mineralogical information

The composition and texture of the core appears heterogeneous under OM (Fig. 3). Modal abundance of minerals and groundmass (determined by point counting) in the core is spatially homogenous. The most abundant material is finely crystalline groundmass + glass, making up 78% of the core, followed by plagioclase (16%), pyroxene (3%), ilmenite (2%) and void space (< 1%).

Augite and plagioclase peaks are identified by XRD in the core. Only peaks consistent with gibbsite and iron oxyhydroxides are observed in the X-ray diffractograms for the bulk rind samples. Diffractograms for the oriented < 2 μm fraction from the rind contain short broad peaks that are consistent with kaolinite. Diffractograms for the soil matrix material contain peaks consistent with halloysite, kaolinite, and vermiculite (+iron oxyhydroxides).

Similar to the findings of previous studies of weathering rinds developed around clasts with basaltic composition cores (e.g., Sak et al., 2004, 2010; Hausrath et al., 2008; Navarre-Sitchler et al., 2011), OM and SEM analyses indicate plagioclase, pyroxene, and the

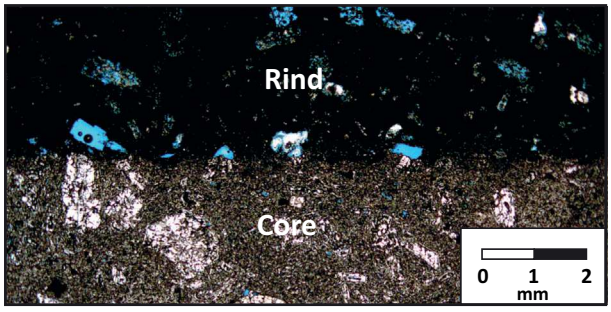

Fig. 3. Representative photomicrograph spanning from the core (lower half of photomicrograph) across the core-rind boundary to the rind (upper half of photomicrograph). The core-rind boundary corresponds with abrupt change in porosity as evidenced by the abundance of blue epoxy filling void spaces. (For interpretation of the references to color in this figure legend, the reader is referred to the web version of this article.)

Table 1
Bulk chemical analyses from transects across the clast and a depth profile through the B horizon.

Sample number	Distance (mm)[a]	Type	SiO_2[b]	Al_2O_3[b]	CaO[b]	Fe_2O_3[b]	K_2O[b]	MgO[b]	MnO[b]	Na_2O[b]	TiO_2[b]	P_2O_5[b]	Total[c]	"LOI"[d]
Core sample														
C1	−10	Core	55.4	20.3	7.77	5.74	0.71	1.81	0.15	3.15	0.81	0.18	96.0	4.0
Rind samples														
R2	1.5	Rind	39.3	25.9	0.16	8.32	0.05	0.46	0.43	0.12	0.87	0.16	75.8	24.2
R3	5	Rind	39.8	27.6	0.15	8.77	0.03	0.32	0.28	0.10	0.77	0.14	78.0	22.0
R4	10	Rind	43.4	23.6	0.13	12.3	0.05	0.21	0.20	0.16	1.17	0.23	81.5	18.5
R5	14	Rind	45.6	22.5	0.13	14.8	0.04	0.17	0.02	0.18	1.53	0.44	85.4	14.6
Rind[e]	–	Rind	42.0	24.9	0.14	11.0	0.04	0.29	0.23	0.14	1.09	0.24	80.2	19.8
Crust sample														
CR6	19	Crust	46.8	21.9	0.15	15.7	0.04	0.16	0.02	0.21	1.85	0.40	87.0	13
Soil samples														
S7	23.5	Soil	46.8	19.1	0.11	14.0	0.10	0.14	0.03	0.22	1.80	0.32	82.6	17.4
S8	28.5	Soil	44.9	12.5	0.57	13.5	0.49	0.35	0.03	0.70	1.76	0.35	75.2	24.8
Soil[e]	–	Soil	45.9	15.8	0.34	13.8	0.30	0.24	0.03	0.41	1.78	0.34	78.9	21.1

[a] Distance measured from the visually defined core-rind boundary and increasing towards the rind-soil interface.
[b] Weight percent of specified oxide. All analyses determined by the Penn State University Materials Characterization Lab using ICP-AES. Detection limit is 0.01 wt %.
[c] Total oxide weight percent sum. Low sums in the rind material may reflect structural water (not measured).
[d] See text.
[e] Mean rind (R2–R5) and soil (S7–S8) composition.

groundmass + glass dissolve completely near the visually defined core-rind boundary. Pyroxene alteration initiates within the ostensibly unweathered core and is characterized by the oxidation of iron around the crystals with no visible porosity as observed at the 10 s of μm scale (Fig. 3). In contrast, plagioclase phenocryst dissolution initiates closer to the core-rind boundary than initiation of pyroxene dissolution, and the plagioclase dissolution reaction is associated with porosity development (Fig. 3). Both minerals dissolve throughout the rest of the rind and porous ghosts of their phenocrysts are visible in the rind under OM.

Porosity quantified from the of blue epoxy pixels in the photomosaic of the thin section varies as function of position. The mean porosity values of the core, rind, crust, and matrix material were determined by analyzing the abundance of blue-colored pixels. Mean porosity in the core is 2.7 ± 1.4%, 3.5 ± 3% in the rind, 4.7 ± 1.3% in crust and 4.7 ± 1.4% in the matrix.

4.3. Chemical compositions

The concentrations of elemental oxides in the core, rind, crust, and matrix are summarized in Table 1. Here, total element concentrations measured in digested rock and weathering product samples by ICP-AES were recast as oxides (wt%). Within the clast, Al_2O_3, Fe_2O_3, and TiO_2 all increase from the core to the rind. In contrast, the concentrations of CaO, K_2O, MgO, Na_2O, MnO, and SiO_2 decrease from the core-rind boundary to the rind, while P_2O_5 remains relatively constant, within the resolution of measurements (Table 1). From the rind through the crust and overlying soil matrix, the concentrations of the analytes remain relatively constant within the resolution of the measurements (0.01 to 0.02 wt%), with the exception of SiO_2, Fe_2O_3, P_2O_5 and TiO_2 which are slightly less abundant in the rind than in either the crust or matrix material (Table 1). In contrast, the concentration of Al_2O_3 decreases from the rind across the crust to the soil matrix (Table 1).

Sums of total oxide bulk concentrations (wt% as measured by ICP-AES) decrease from the core (96%) to the rind (80.2%), crust (87%), and matrix (78.9%). Following Sak et al. (2010), the difference between 100% and the measured total weight percent is interpreted to represent loss of organic matter or waters of hydration during the metaborate fusion. These values are analogous to "loss on ignition" (LOI), which is commonly reported after ashing a sample at 900 °C prior to Li metaborate fusion (during Li metaborate fusion the sample is heated to 900 °C but Li metaborate is added as flux). The calculated differences are 14.6 to 24.2% across the rind, 13% in the crust and 17.4 to 24.8% in the matrix. These differences are interpreted as loss of waters of hydration within clay (labeled as "LOI" in Table 1).

The presence of porosity and hydrated phases in the section also cause the total weight percent of EMP analyses to be < 100%. The difference between 100% and the total weight percent of oxides is considered here as the "porous hydrated fraction" (PHF). For the same sample analyzed under ICP-AES or EMP, Sak et al. (2010) called the difference between the PHF and "LOI" values the residual, which is used as a proxy for high-resolution variations in porosity.

To explore if this measurement of PHF and LOI revealed porosity, a sample of disaggregated and homogenized weathering rind was analyzed with and without black pepper. In one of the samples, a known volume of micro-milled black pepper was added. Then the sum total oxide (wt% as measured by ICP-AES) was determined for both samples and the LOI was calculated as discussed above. For comparison, ten spot analyses of that same rind, rind + pepper, and pepper material were analyzed on the EMP at various spot sizes to determine PHF. In all trials of a specific medium, the mean measured PHF vary by < 3%; and at a spot size of 100 μm the standard deviations about that mean is < ~2%. Consequently, porosity estimates calculated using this methodology is presumed to represent porosity at the 100 μm scale.

Chemical and mineralogical changes are also documented in SEM-EDS images of the core-rind boundary (Fig. 4). At the core-rind boundary, phenocrysts transition from unaltered on the core side to partial or complete alteration in the rind. Some of the plagioclase grains

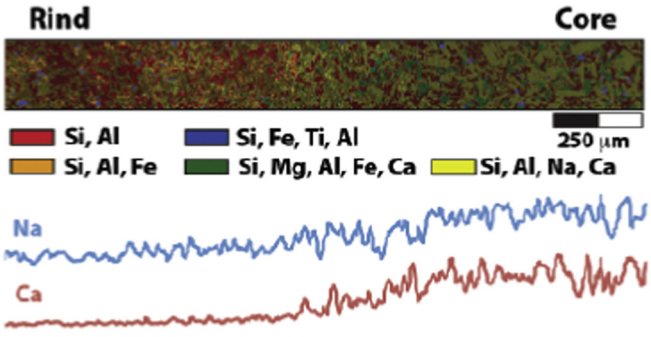

Fig. 4. SEM-EDS false color map spanning the core-rind boundary (see Fig. 2b for location). The image is color coded by elemental phase. EDS values are averages of net intensity across the image. Na and Ca are a proxy of plagioclase dissolution, indicating a reaction front width of 550 μm and 450 μm, respectively.

Table 2
U and Th concentrations and activity ratios.

Distance (mm)[a]	Type	U (μg/g)	(^{234}U/^{238}U)	±	Th (μg/g)	(^{230}Th/^{232}Th)	±	(^{238}U/^{232}Th)	±	(^{230}Th/^{238}U)	±
−10	Core	0.745	1.016	0.005	1.997	1.016	0.010	1.141	0.014	0.891	0.009
1.5	Rind	1.184	1.022	0.005	2.793	1.019	0.010	1.296	0.016	0.786	0.008
5	Rind	1.164	1.023	0.005	2.820	1.045	0.010	1.261	0.015	0.829	0.008
14	Rind	1.168	1.044	0.005	2.386	1.227	0.012	1.495	0.018	0.821	0.008
19	Crust	0.674	1.025	0.005	1.598	1.218	0.012	1.288	0.015	0.946	0.009
23.5	Matrix	0.356	1.018	0.005	1.167	1.047	0.010	0.931	0.011	1.124	0.011
28.5	Matrix	0.426	1.015	0.005	1.239	1.063	0.011	1.051	0.013	1.011	0.010

[a] Distance measured from the visually defined core-rind boundary and increasing towards the matrix material.

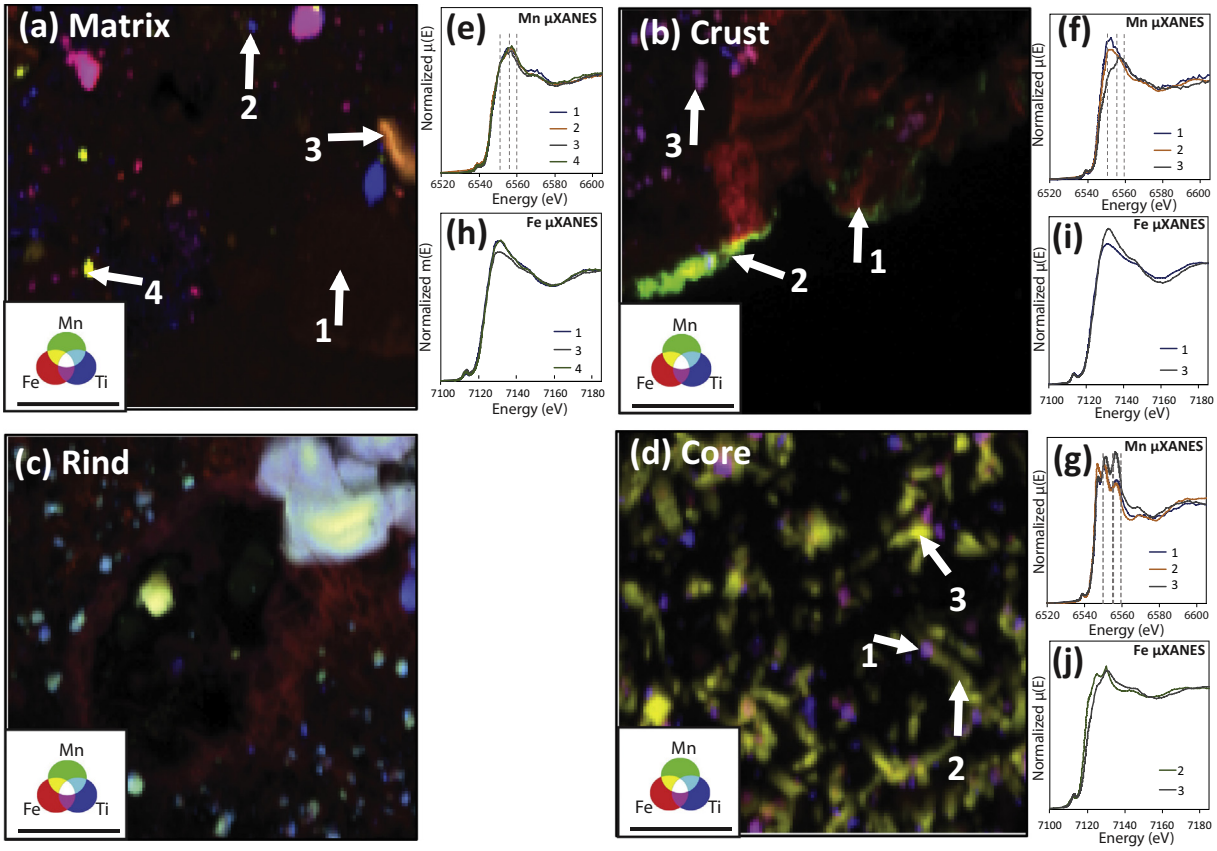

Fig. 5. Micro-X-ray fluorescence maps for the (a) matrix, (b) crust, (c) rind, and (d) core regions. These maps show the spatial distribution and relative intensities of Fe (red), Mn (green), and Ti (blue) fluorescence within each region. Combinations of the elements appear as yellow (Fe + Mn), purple (Fe + Ti), cyan (Mn + Ti), or white (Fe + Mn + Ti), as indicated by the color wheel in the inset. Black areas indicate voids and fractures where these elements were not present. The scale bar (black horizontal line) is 100 μm. The map was collected at 7100 eV with a 2 × 2 μm focused beam, 3 μm step size, and 30 ms/pixel dwell time. Micro-XANES spectra (e–g) at the Mn K-edge (e–g) and Fe K-edge (h–j) are plotted for each point of interest indicated by an arrow in the XRF maps. Vertical dashed lines indicate the absorption white line energies for reference Mn(II), Mn(III), and Mn(IV) compounds, and Fe(II) and Fe(III) compounds (from left to right). (For interpretation of the references to color in this figure legend, the reader is referred to the web version of this article.)

are porous. Interiors of these porous plagioclase ghosts contain an Al-rich solid, consistent with plagioclase weathering to gibbsite. Ca and Na intensities were measured with EDS and averaged vertically across the entire SEM-EDS maps and are plotted in Fig. 4. These EDS profiles are calculated with a three-point moving average to smooth compositional jumps at boundaries. The Ca and Na line that traverses across the core-rind boundary documents that the loss of these two elements along the transect are correlated (Fig. 4), consistent with the OM observation that plagioclase dissolution occurs coincident with the core-rind boundary and is associated with initial porosity development. Concentrations of Ca and Na decrease in a narrow zone (≤550 μm wide). In addition, partially dissolved plagioclase phenocrysts and pyroxene are present beyond the zone of Ca and Na change.

Porosity, color, and elemental concentrations are each relatively uniform within a given part of the weathering clast: the core, the rind, or the soil matrix. All of the reaction is limited to the transitions between these zones. The transition zone at the core-rind interface is referred to as the weathering reaction front (Figs. 3 and 4).

4.4. U-series isotope compositions

U and Th concentrations of the drilled samples of core were 0.745 and 1.997 μg/g, respectively (Table 2). While the rind has a higher concentration of U and Th than the core, ranging from 1.164–1.201 μg/g for U and 2.386–2.820 μg/g for Th, the indurated crust (0.674 μg/g U and 1.598 μg/g Th) and the matrix material (0.356–0.426 μg/g U and 1.167–1.238 μg/g Th) have lower concentrations of U and Th than the core and rind.

The core activity ratios for ($^{234}U/^{238}U$) and ($^{230}Th/^{238}U$) are 1.016 and 0.891, respectively. Parentheses will be used to denote activity ratios hereafter. These U-series activity ratios are slightly different from the secular equilibrium values within errors as expected for ~ > 1.25 Myr old parent material, probably due to the younger age of the basaltic andesite bedrock in the region (e.g., ~620 ka, Samper et al., 2007). Nonetheless, the ($^{234}U/^{238}U$) increases systematically from 1.022 to 1.044 in the rind, but then decreases to 1.025 in the crust and further to 1.015 in the uppermost matrix sample (Table 2). The ($^{238}U/^{232}Th$) value is 1.141 in the core and increases generally from 1.261 to 1.495 in the rind, then decreases from 1.288 in the crust to 0.931 and1.051 in the matrix (Table 2). ($^{230}Th/^{232}Th$) values in the core, rind, crust and matrix follow a similar trend as ($^{238}U/^{232}Th$). The ($^{230}Th/^{238}U$) values show an opposite trend to ($^{238}U/^{232}Th$), values decrease from the core (0.891) to the rind (0.786–0.821) and then increases to the crust (0.946) and the matrix (1.011 and 1.124).

The trends of ($^{238}U/^{232}Th$) and ($^{230}Th/^{232}Th$) ratios as a function of distance from the core-rind boundary reflect the changes of U-series mass balance due to processes such as addition and loss of ^{234}U and ^{238}U and decay of U-series isotopes with time during rind and regolith formation (Ma et al., 2012; Engel et al., 2016). Such trends are used in the following discussion to determine the timescales of rind and matrix formation.

4.5. Spectroscopic information

Micro-X-ray-fluorescence (μXRF) maps indicate differences in the microscale distributions of Fe and Mn between the core and the rind, crust, and matrix (Fig. 5). Two different phases containing Fe and Mn were observed in the core (Fig. 5d): 1) elongate crystals that were relatively enriched in Fe and Mn; and 2) round, Ti-rich crystals (~10–30 μm diameter grains) that contained relatively minor proportions of Fe and Mn. In contrast, Fe was evenly distributed throughout the rind, crust, and matrix, consistent with precipitation of residual iron oxyhydroxides derived from weathering of primary minerals. Iron-rich precipitates were observed to often surround voids in the rind where primary minerals were presumably dissolved during weathering (Fig. 5c). Notably, a thin (~40 μm) Mn-rich zone was prominent along the fractures between the rind and the crust (Crust-1 region; Fig. 5b) and between the crust and the matrix (Crust-2 region). Iron was also slightly enriched in the Mn-rich zone in Crust-1 relative to the rind. Mn fluorescence along the fracture in Crust-2 swamped the Fe Kα signal; therefore, no inferences about Fe could be made for this region.

Concentrations of MnO decreased from 0.15 (wt%) in the core to 0.02 (wt%) in the crust (Table 1) and Fe_2O_3 increased from 5.74 (wt%) in the core to 15.7 (wt%) in the crust (Table 1). Manganese and Fe were more oxidized in the weathered rind, crust, and matrix than in the unweathered core based on linear combination fits of Mn and Fe K-edge XANES spectra. The average oxidation states of Mn (2.0 ± 0.1; n = 3) and Fe (2.0 ± 0.3; n = 2) in the core were consistent with the occurrence of divalent metal cations in primary silicate minerals. The Fe adsorption edge was shifted to a slightly higher energy in Core spot 3 relative to spot 2 (Fig. 5j), possibly due to an increasing contribution of Fe(III) generated from initial oxidation of Fe(II) contained in pyroxene. In core spot 2, an E_0 value < 2 may result from an absorption edge for Fe that is lower energy than the Fe(II)-oxide standards; indeed, the Fe absorption edge for spot 2 is intermediate between iron (II) sulfides (~7117 eV) and iron (II) oxides and silicates (~7120 eV) (O'Day et al., 2004).

Oxidation states were also determined for Mn and Fe at two locations each in the rind and crust and one location in the soil matrix (Table 3, Fig. 6). The average oxidation states across the weathered materials were also determined for Mn (2.6 ± 0.2; n = 17) and Fe (2.8 ± 0.1; n = 15) (Fig. X). All of the values in the weathering products were higher than the average oxidation states for Mn (1.97 ± 0.1; n = 3) and Fe (1.97 ± 0.3; n = 2) in the core, consistent with oxidation of these elements from core to the weathering products (Fig. X). Manganese was slightly more reduced in the Mn-rich zones of Crust-1 (2.3 ± 0.1; n = 2) and Crust-2 (2.6 ± 0.1; n = 3) relative to the Mn-poor zones in the rind (2.6 ± 0.1; n = 5), crust (2.8 ± 0.1; n = 3) and regolith (2.8 ± 0.1; n = 4) regions (Figs. 5 and 6).

Table 3
Fe and Mn oxidation states as a function of position.

Sample	Distance (mm)	Mn oxidation state	n	Fe oxidation state	n
Core	−0.5	1.97 ± 0.08	3	1.97 ± 0.32	2
Rind 1	6.2	2.60	1	2.83 ± 0.03	2
Rind 2	11.9	2.55 ± 0.10	4	2.77 ± 0.08	4
Crust 1	19.7	2.50 ± 0.29	3	2.80 ± 0.11	2
Crust 2	21.3	2.70 ± 0.13	5	2.85 ± 0.04	4
Matrix	25.6	2.76 ± 0.04	4	2.78 ± 0.06	3

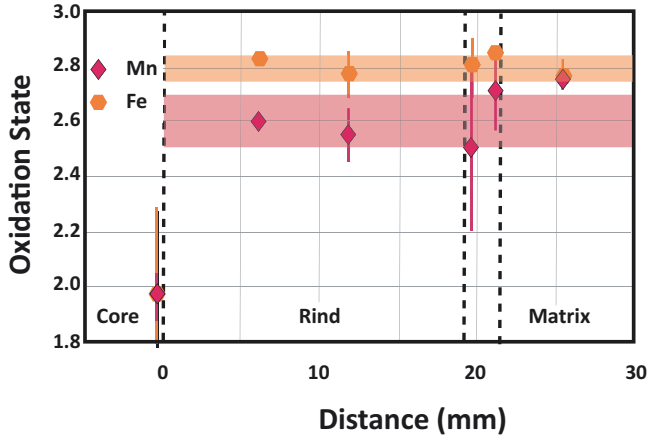

Fig. 6. Average oxidation state of Mn and Fe as a function of distance from the core point, which was collected within 150 μm of the core-rind boundary. Oxidation states were calculated using linear combination fits to a suite of Mn and Fe bearing standards. Each point represents the average ± standard deviation of multiple XANES measurements collected within a 0.02 mm^2 area.

5. Discussion

The observations are used to formulate chemically-based models for weathering rind development. ICP-AES mass balance calculations are first used to quantify elemental mobility and characterize mineral reaction sequences across the core, rind, crust, and soil matrix. Second, EMP and ICP-AES data are combined to constrain changes in porosity at a finer spatial resolution than is possible with image analysis. These results are then compared with theoretical predictions of spatial trends in porosity as a function of interaction among reaction fronts (Lebedeva et al., 2007, 2015). Third, variations in U-series behavior inside the rind portion of the sample provide information of rates and duration of rind formation. Furthermore, variations in U-series behavior between the rind and regolith are evaluated in the context of changes in redox state across the rind-regolith continuum. Finally, to assess the role of climatic variations this sample is compared to previously studied samples and to watershed-scale weathering rates of Basse-Terre Island.

5.1. Mass balance calculations

To interpret the weathering reactions through the core, rind, and soil matrix, the open system elemental mass transfer coefficient, $\tau_{i,j}$, is calculated (Brimhall and Dietrich, 1987; Brimhall et al., 1991). Ti and Th are known as an immobile element (i) in tropical settings when organic acid concentrations are minimal (i.e., Barshad, 1964; Marshall, 1977; Milnes and Fitzpatrick, 1989; White, 1995; White et al., 1998;

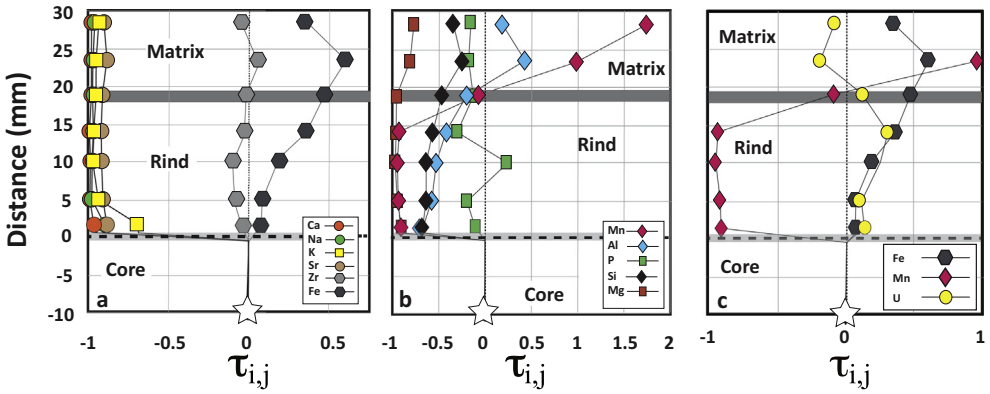

Fig. 7. Elemental mass transfer $\tau_{i,j}$ calculated using Eq. (1) plotted as a function of position relative to the core-rind boundary at 0, increasing towards the matrix, derived from bulk ICP-AES data. Light gray bar at 0 mm distance in A.B, and C represents a ~1000 μm thick reaction front. In A and B, Ti is assumed to be immobile, in C Th is the immobile. Negative values of $\tau_{i,j}$ imply loss of the element j (-1 represents 100% loss) relative to the core composition.

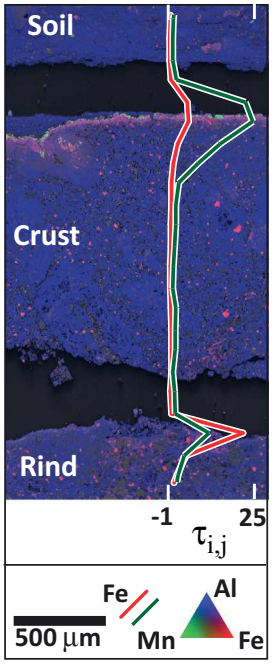

Fig. 8. False color elemental map spanning the crust region (see Fig. 2b for location). The image is color for the relative concentrations of elements: green is Mn, blue is Al, and red is Fe. Overlain on the image are $\tau_{i,j}$ values. Negative values of $\tau_{i,j}$ imply loss of the element j (-1 represents 100% loss) and positive $\tau_{i,j}$ imply enrichment relative to the core composition. (For interpretation of the references to color in this figure legend, the reader is referred to the web version of this article.)

Sak et al., 2004; Ma et al., 2012). Because of this, concentrations of Ti or Th can be compared relative to concentrations of a mobile element (*j*) to determine the loss or gain of element *j*:

$$\tau_{i,j} = \frac{c_{j,w} c_{i,p}}{c_{j,p} c_{i,w}} - 1 \quad (1)$$

Here, *p* is defined as the parent material, in this case the core, and *w* is defined as the weathered material, in this case the rind, crust, and regolith. When $\tau_{i,j} = 0$, the element *j* is immobile with respect to *i*. Positive $\tau_{i,j}$ values indicate enrichment of *j* relative to the core, while negative $\tau_{i,j}$ values indicate depletion relative to the Ti (Fig. 7a and b) and Th (Fig. 7c and d) in the core. When $\tau_{i,j} = -1$, the element *j* has been completely removed during the weathering process. The values of $\tau_{i,j}$ for each element are plotted as a function of distance from the visually defined core-rind boundary (Fig. 7).

Sampling logistics in previous studies limited the $\tau_{i,j}$ analyses to changes spanning the core-rind boundary. The order of elemental loss across the core-rind boundary in previous clast samples was: Ca ≈ Na > K ≈ Mg > Si > Al > Fe ≈ P > Ti = 0 (i.e., Sak et al., 2004, 2010). Here we use $\Sigma\tau_{i,j}\Delta z$ where Δz is the thickness interval between each sampling point to quantify enrichment (or depletion) across the entire weathering clast (rind and crust). Similarly, the relative loss sequence from the core to the crust is: Ca > Na ≈ Mg > K > Mn > Si > Al > Ti = 0 > P > Fe. Both P and Fe shows enrichment (> 0) away from the core-rind boundary into the rind, crust and matrix (Fig. 7). However, in the case of this sample, Ca, Na, K, and Sr are all characterized by depletion profiles from the core-rind boundary across the crust into the matrix. In contrast, Mn, Al, Ba, Si, and Mg exhibit depletion from core to rind and enrichment from the rind to the matrix (Fig. 7a and b). For these elements, $\tau_{i,j}$ values decrease to ≤ -0.6 within a narrow (≤1.5 mm wide) reaction front extending from the visually defined core-rind boundary where the first bulk sample of analyzed rind material. This estimate of an abrupt boundary is based upon the assumption that no depletion occurs coreward of the core-rind boundary. A narrow and abrupt reaction front is consistent with OM observations, and previous mass balance investigations of weathering rinds developed around low porosity basaltic composition cores (Sak et al., 2004, 2010; Hausrath et al., 2008; Navarre-Sitchler et al., 2011).

Unlike the $\tau_{i,j}$ data shown in Fig. 7a and b, Th is used as the immobile reference element in Fig. 7c. The $\tau_{i,j}$ data for Fe and Mn are similar when referenced to Ti or Th (Fig. 7a-c). The choice of immobile element is also consistent with analyses of previous clasts collected on Basse-Terre island (Sak et al., 2010; Ma et al., 2012; Engel et al., 2016). The SEM-EDS-derived dataset allows us to test the previous assumption that elemental loss does not initiate coreward of the core-rind boundary (Fig. 4). These data suggest that elemental loss of Ca and Na, attributed to plagioclase dissolution initiates coreward of the visually defined core-rind boundary (Fig. 4). The reaction front at the core-rind boundary is abrupt (< 2.1 mm thick) for all elements analyzed.

In contrast to the rind, the crust is enriched in K and Mg compared to the weathering rind (Fig. 7). The matrix material is characterized by greater variability but overall less depletion than the weathering rind. Variability in the matrix is attributed to the large grain size relative to the spot size.

SEM-EDS images of crust also document changes in chemistry (Fig. 8). The outer (upper) edge of the weathering rind is marked by a narrow localized veneer characterized by extreme Fe enrichment with $\tau_{Ti,Fe} > 20$, and the outer edge of the crust by $\tau_{Ti,Mn} \geq 25$ (Fig. 8). Development of a thin Mn-rich veneer on the upper surface of the crust is consistent with the μXRF mapping (Fig. 5c).

5.2. Porosity

Increases in porosity from the core to the rind are attributed largely to plagioclase and glass dissolution (Fig. 3), and residual values plotted as a function of distance from the core-rind boundary (Fig. 9) clearly demonstrate the lower porosity of the core compared to the rind, crust,

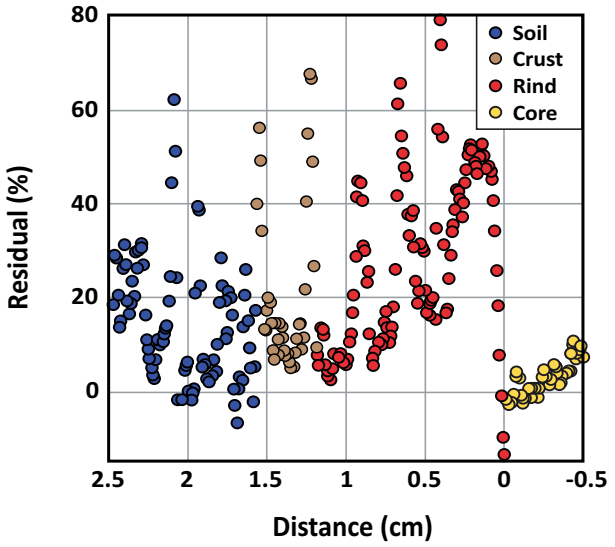

Fig. 9. Residual values as a function of distance from the core-rind boundary. Negative values are due to variability in porosity and averaged LOI values. A sharp increase in porosity indicates the core-rind boundary, which porosity measurements indicate an abrupt (900 μm) wide reaction front. The two sharp increases in porosity mark the edges of the crust.

and soil matrix.

Within the core, porosity as quantified by image analysis and calculated residual values display similar spatial trends. The residual values and porosity decrease approaching the core-rind boundary from greater distances within the core followed by abrupt increases across a narrow (< 900 μm wide) reaction front coincident with the visually defined core-rind boundary. This reaction front is co-located with first appearance of ghosted plagioclase phenocrysts within the core and is approximately the same width as the length of the long dimension of the phenocrysts. The colocation of the porosity reaction front with plagioclase dissolution and the lack of porosity coincident with the pyroxene oxidation deeper in the core attest to a different mechanism of porosity formation than has been proposed for the Rio Blanco quartz diorite within Rio Icacos watershed of Puerto Rico. In that rock, the positive ΔV of reaction associated with Fe oxidation (in that case biotite) is inferred to result in the accumulation of elastic strain and eventual fracturing and porosity production (Buss et al., 2008). Apparently, oxidation of pyroxene is not resulting in fracturing in this clast.

Spatial patterns in the distribution of porosity and residual within the weathered material (rind, crust and matrix) differ from those in the core. Most notably, residual values in the weathered materials are more variable (Fig. 9). This is attributed to the repeated probing of the large phenocryst ghosts in the weathered material (Fig. 3). Within the weathered materials the boundaries between both the rind-crust and crust-matrix are marked by parallel, narrow (< 200 μm wide) fractures (Figs. 2b and 7).

5.3. Weathering rates

Due to the planar, parallel nature of the core-rind and rind-crust boundaries that we studied (Fig. 2b), weathering rates across these boundaries are consistent across the sample, and unlike previously studied samples, curvature does not have to be considered (Sak et al., 2010; Ma et al., 2012; Lebedeva et al., 2015; Engel et al., 2016). Exposures of volcanic flows in the Lezarde watershed within the immediate vicinity of the sample sites are $^{40}Ar/^{39}Ar$ dated at ~620 ka (Samper et al., 2007), indicating that the duration of weathering must be ≤620 ka. Rind formation processes modify U-series activity ratios such that the ^{238}U-^{234}U-^{230}Th-disequilibria can be used to determine rind formation ages and weathering rates (Pelt et al., 2008; Ma et al., 2012). Th phases are typically insoluble, so Th is generally immobile and particle-reactive during water-rock interactions (Rosholt et al., 1966; Latham and Schwarcz, 1987a, 1987b; Gascoyne, 1992; Chabaux et al., 2003), especially in tropical climates (Ma et al., 2007; Pelt et al., 2008; Ma et al., 2012). Uranium contrasts Th with its mobility during water-rock interactions in oxidizing conditions (Chabaux et al., 2003). The observed ($^{234}U/^{238}U$) values of the rind samples in the studied clast range from 1.022 to 1.044, consistent with two important processes during rind formation: (1) chemical leaching that generates ($^{234}U/^{238}U$) ratios < 1 in the solid weathering products; and (2) continuous addition of U as a precipitate or sorbate from soil pore waters with ($^{234}U/^{238}U$) ratios > 1, which results in excess ^{238}U and ^{234}U in the rind materials. Both U addition and leaching processes during chemical weathering modify the ($^{234}U/^{238}U$) activity ratios in the rind. Over time, the excess ^{234}U (half-life, $T_{1/2}$ = 244 kyr) decays to ^{230}Th ($T_{1/2}$ = 75 kyr). The subsequent radioactive production of ^{230}Th and the immobile behavior of Th isotopes account for the observed continuous increase of ($^{230}Th/^{232}Th$) activity ratios for the rind profile. With an open-system U-series mass balance model that allows for continuous chemical leaching and addition of U-series isotopes during rind formation (Dequincey et al., 2002; Ma et al., 2012 and references therein), the changes of U-series isotopes with time in the rind can be modeled as:

$$\frac{d^{238}U}{dt} = f_{238} - \lambda_{238}{}^{238}U - k_{238}{}^{238}U \quad (2)$$

$$\frac{d^{234}U}{dt} = f_{234} + \lambda_{238}{}^{238}U - \lambda_{234}{}^{234}U - k_{234}{}^{234}U \quad (3)$$

$$\frac{d^{230}Th}{dt} = \lambda_{234}{}^{234}U - \lambda_{230}{}^{230}Th \quad (4)$$

$$\frac{d^{232}Th}{dt} = -\lambda_{232}{}^{232}Th \quad (5)$$

Here, ^{238}U, ^{234}U, ^{230}Th, and ^{232}Th are the concentration terms (atoms g^{-1}) in the rind; terms λ_{238}, λ_{234}, λ_{230}, and λ_{232} are the decay constants for ^{238}U, ^{234}U, ^{230}Th and ^{232}Th (yr^{-1}); f_{238} and f_{234} are the addition rates of ^{238}U and ^{234}U into the rind (atoms g^{-1} yr^{-1}). The f terms lump together all the processes that add U isotopes into the rind material such as precipitation and adsorption of U from soil water, separate from radioactive production. The f terms are assumed to be constant with time for the purpose of simplicity and tractability of the model (Ghaleb et al., 1990; Dequincey et al., 2002; Ma et al., 2012). The close-to-linear increase of ($^{238}U/^{232}Th$) ratios with distance from the core into the rinds along the analyzed transect is consistent with the assumption of constant U input rate (f terms) in the model. The terms k_{238} and k_{234} are first-order rate constants (yr^{-1}) for chemical leaching of ^{238}U and ^{234}U from U-containing phases (Latham and Schwarcz, 1987a, 1987b; Plater et al., 1992; Vigier et al., 2001), i.e. the U release rates equal $k_{238}{}^{238}U$ and $k_{234}{}^{234}U$. For a given rind sample, t is the rind formation age (in years). For the studied rind samples, measured ($^{238}U/^{232}Th$), ($^{230}Th/^{232}Th$), and ($^{234}U/^{238}U$) activity ratios were used as input values to solve unknown parameters (f_{238}, f_{234}, k_{238}, k_{234}, and individual t) with an inverse Monte-Carlo algorithm (Engel et al., 2016). The core U-series compositions (Table 3) were used as the initial composition in the model. U-series dating indicates that the rind ages increases away from the core-rind boundary: 7.1 ± 1.8 ka at a distance of 1.5 mm from the boundary, 9.2 ± 2.1 ka at 5 mm, and 66.6 ± 4.3 at 14 mm (Fig. 10; with fitting parameters $f_{238U}/^{238}U_0 = 7.8 \pm 1.6 \times 10^{-5}\,yr^{-1}$, $f_{234U/238U} = 1.09 \pm 0.04$, $k_{238U} = 5.9 \pm 1.2 \times 10^{-5}\,yr^{-1}$, $k_{234U}/k_{238U} = 1.05 \pm 0.05$; Details of the U-series model is presented in Ma et al., 2018). The age of the overlying indurated and fractured crust is ~72 ka assuming it followed the same U-series model as the weathering rind. If the rate of rind

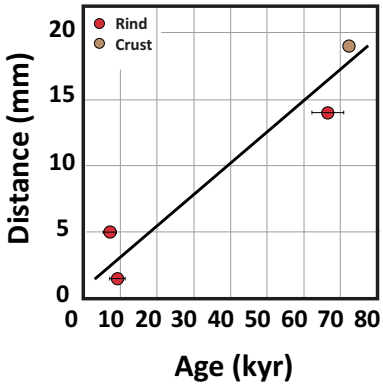

Fig. 10. Plot of U-series ages calculated at different distances from the core-rind boundary in the weathering rind and crust. Age in the weathering rind increases away from the core-rind boundary to a maximum of 66 ka 19 mm from the core-rind boundary. The surrounding crust (21 mm from the core-rind boundary) is 72 ka. A linear regression through these data yield a mean rind formation rate of ~0.21 ± 0.15 mm kyr^{-1}.

advance is assumed constant in time (Sak et al., 2004; Pelt et al., 2008), the calculated rind advance rate for this clast is ~0.21 ± 0.15 mm kyr^{-1}(Fig. 10; it is noted that the uncertainties of rind ages were not incorporated into the uncertainties of the rate calculation as the large scatters on the age-distance trend and the limited number of ages contribute to the uncertainties of the rind advance rate). A recent laser ablation U-series isotope study conducted on the same weathering rind (AN-14-3.2; Ma et al., 2018) yielded a rind advance rate of 0.29 ± 0.11 mm kyr^{-1}, in agreement with the rate reported in this study.

5.4. Weathering advance rates across scales and gradients in mean annual precipitation

The entire island of Basse-Terre is constructed of Pliocene to recent andesitic volcanics which decrease in age from north to south, parallel to the topographic divide (Sampler 2007, Fig. 1b and c). Superimposed on this age trend is a pronounced east-west orographic precipitation effect (Fig. 1b). This configuration makes Basse-Terre a suitable site for field investigations seeking to isolate the effects of bedrock age and precipitation on the chemical weathering. Previous studies have constrained chemical weathering rates at the scale of weathering clasts (Ma et al., 2012; Engel et al., 2016) and the watershed (Gaillardet et al., 2011) across Basse Terre Island.

Specifically, Engel et al. (2016) compared weathering rind advance rates calculated across low curvature segments of the core-rind boundary of clasts collected from the high precipitation Bras David (MAT = 23 °C and MAP = 3400 mm yr^{-1}) watershed (Ma et al., 2012) and the relatively low precipitation Deshaies (MAT = 23 °C and MAP = 1800 mm yr^{-1}) watershed (Fig. 1b). Engel et al. (2016) found that variations in the chemical weathering rate measured at the clast scale was similar to that measured using water chemistry at the catchment scale. The rind advance rate of 0.21 ± 0.15 mm kyr^{-1} calculated in this study across the 19 mm thick weathering rind from the Lezarde watershed (MAT = 25 °C and MAP = 4500 mm yr^{-1}) compares favorably with the rind advance rate of 0.18 ± 0.07 mm kyr^{-1} calculated across the low curvature segment of the clast collected from the Bras David watershed. The rind advance rate calculated for the < 120 ka clast collected from within the Deshaies watershed is ~60% slower than those calculated for clasts from the < 120 ka Bras David and < 60 ka Lezarde watersheds. Similarly, Gaillardet et al. (2011) calculated a catchment-wide chemical weathering rate of 46 t/km^2/yr in the Deshaies watershed and 92 and 101 t/km^2/yr, respectively in the Bras David and Lezarde watersheds. In other words, the catchment-wide chemical weathering rate derived from the solute chemistry of the Deshaies watershed is ~50% slower than the Bras David and Lezarde watersheds.

Clast-scale formation rates are constrained using the chemistry of the rind materials and represent rates integrated over ~75 kyr timescales. In contrast, the catchment scale weathering rates are derived from riverine fluxes and reflect short term chemical weathering rates. Although the magnitudes of precipitation have likely varied over the ~75 kyr interval recorded by the weathering clasts, the persistence of spatially consistent weathering rates when comparing solute- and residuum-derived rates argue for a long-lived gradient in MAP across Basse-Terre Island.

In addition to documenting a persistent spatial gradient in weathering rates across Basse-Terre, Engel et al. (2016) showed that the weathering rates measured across low curvature segments of the core-rind boundary of clasts from the Bras David and Deshaies watersheds are ~2000 times slower than the catchment scale weathering rates calculated for the host catchments. This discrepancy was anticipated and has, in the literature, been attributed to differences in how surface areas are measured using different "rulers" at different spatial scales (e.g., Navarre-Sitchler and Brantley, 2007). Employing the same methodology as Engel et al. (2016), the clast-derived weathering rate is ~2000 times slower than the catchment derived chemical weathering rate. These analyses independently verify the findings of Engel et al. (2016) while adding an additional clast and catchment scale data point to the regional compilation.

5.5. Redox reactions involving Mn species

Manganese accumulation in the crust (Fig. 4) and its enrichment profile (Figs. 5 and 6) are consistent with precipitation of Mn oxide minerals from aqueous solutions containing Mn. We reconcile the net Mn depletion ($\Sigma\tau_{Mn}\Delta z = -1.77$) and Mn retention in the crust to the immobilization of Mn leached from core minerals and oxidized at the crust interface. Given Fig. 7 in which it is clear that the rind is largely depleted of Mn, it is unlikely that the Mn in the crust is oxidized Mn from the rind. Instead, Mn-oxide accumulation is the likely mechanism for Mn enrichment in the crust.

Such Mn may also provide a reactive surface for U immobilization (discussed below). However, abiotic oxidation of aqueous Mn^{2+} is kinetically limited in the acidic environment we expect for the clast (Diem and Stumm, 1984; Stumm and Morgan, 1996). It is widely accepted that many natural Mn oxides are formed by the microbial oxidation of Mn^{2+} (e.g., Bargar et al., 2005; Tebo et al., 2004; Webb et al., 2005), and the oxidation of Mn(II) by microorganisms is many orders of magnitude faster than abiotic reactions (e.g. Tebo et al., 2004, 2005; Morgan, 2005). Many studies have demonstrated that microorganisms readily oxidize Mn(II) in alkaline environments and circumneutral environments when the conditions are oxic and hypoxic (e.g. Chapnick et al., 1982; Villalobos et al., 2003; Santelli et al., 2010, 2011), or even in acidic environments (pH ~4.5) where Mn^{2+} is the thermodynamically stable species (Ivarson and Heringa, 1972; Akob et al., 2014; Mayanna et al., 2015). It is therefore possible that Mn-oxidizing bacteria near the surface of the clast have led to the Mn-oxide accumulation along the crust boundaries. On the other hand, iron oxide minerals in the crust could also have promoted abiotic precipitation of Mn oxide minerals such as manganite (γ-MnOOH), feitknechtite (β-MnOOH), and hausmannite (Mn_3O_4) (Wang et al., 2015; Lan et al., 2017). Surfaces of Fe oxide minerals such as ferrihydrite and goethite can sorb Mn^{2+} ions and catalyze oxidation by O_2; which may occur in transient circumneutral conditions.

Manganese oxidation states in the rind, crust, and matrix (ranging from 2.3 to 2.9) were more reduced than expected given that oxidizing weathering environments are typically dominated by Mn(III,IV)-oxides such as birnessite and todorokite (Post, 1999; Tebo et al., 2004; Akob et al., 2014; Mayanna et al., 2015). Instead, these precipitates are more

consistent with a Mn(II,III)-bearing phase such as hausmannite. This mineral is typically found in hydrothermal and metamorphic deposits (Post, 1999) but has also been identified as a product of Mn-oxidation by ferrihydrite (Wang et al., 2015) and in the presence of microorganisms (Mann et al., 1988) in circumneutral environments. Low-valence Mn-oxides may form when high concentrations of Mn^{2+} are present in solution (Hastings and Emerson, 1986; Mann et al., 1988) and serve as intermediates in the transition to more oxidized phases (Murray et al., 1985; Hastings and Emerson, 1986). Manganese oxides could also have been partially reduced by aqueous Fe^{2+}, lowering the average Mn oxidation state and facilitating precipitation of iron oxides along the crust (Schaefer et al., 2017). Alternatively, average oxidation states measured across all parts of the rind-crust-regolith are consistent with values obtained for bulk soils in acidic environments (Herndon et al., 2014; Keiluweit et al., 2015), and could reflect mixtures of Mn-bearing phases (e.g., oxides, clays, organic matter) containing different Mn oxidation states.

Manganese oxide formation along the fractures may also influence the distribution of U within the clast. Uranium exhibits an addition profile in the weathered rind crust and depletion in the soil matrix (Fig. 7c), suggesting input of U from the regolith matrix. Soil water that percolates through fractures in the clast may contain mobile U(VI) that subsequently adsorbs to or is incorporated into Fe-hydroxides.

5.6. Fe enrichment trends

The diagnostic brownish yellow color of the weathering rind that distinguishes the clast from the surrounding weathering profile is attributed to iron oxide phases such as goethite, α-FeO(OH), that form through weathering reactions in lateritic soils. Iron enrichment is evident across the rind, crust as evidenced by the positive $\Sigma\tau_{Fe}\Delta z$ value of 0.50., corresponding to previous research of weathering rinds within soil profiles (Sak et al., 2004, 2010; Navarre-Sitchler et al., 2011; Yoshida et al., 2011), indicating an additional source of Fe other than the core. The dissolution of the augite, ilmenite, and groundmass + glass phases in the core produce $FeO(OH)_{(s)}$ and $Fe^{2+}_{(aq)}$. As the weathering reaction front advances coreward, the solid FeO(OH) produced from the dissolution of augite remains immobile and accumulates in the rind. At the same time, $Fe^{2+}_{(aq)}$ from ilmenite and groundmass + glass dissolution leaches from surrounding soil matrix and accumulates as iron oxides in the rind. The combination of solid and aqueous Fe phases produced through weathering of clast minerals and through oxidation of infiltrating dissolved $Fe^{2+}_{(aq)}$ generates the enrichment trend in the rind progressing outward from the core, with increasing $\tau_{i,j}$ values. Similarly, although both Si and Al are depleted in the rind relative to the core, their $\tau_{i,j}$ values show maximum depletion near the core-rind boundary and become less negative towards the outer clast (Fig. 7), suggesting addition from the surrounding matrix.

6. Conclusions

To further investigate weathering reactions at the scale of a clast, we systematically investigated a single sample that spans from the unweathered andesitic composition core, across the weathering rind and into the surrounding soil matrix material over a distance of < 5 cm. The sample is subdivided into four components: the unweathered core, weathering rind, crust, and soil matrix by visual inspection. The sample was characterized by petrographic, bulk chemical, electron microprobe, ablation inductively coupled plasma-mass spectrometer, U-series isotope analyses, X-ray microprobe analyses, and micro-X-ray absorption near edge structure spectroscopy.

Major element analyses combined with EMP and LA-ICP-MS transects constrain the extent of elemental loss associated with rind formation and elemental transitions coincident with the rind-crust and crust-matrix boundaries. Similar to previously studied clasts, the elemental loss associated with rind formation occurs over a narrow (< 900 μm) zone and decreases in the order Ca > Na ≈ Mg > K > Mn > Si > Al > Ti = 0 > P > > Fe, suggesting the sequence of weathering reactions as: glass + groundmass matrix and primary minerals (plagioclase and pyroxene) weather to produce Fe oxyhydroxides, gibbsite and minor kaolinite. Petrographic and EMP analyses suggest that the reactivity of phases decrease in order from plagioclase ≈ pyroxene ≈ glass matrix ≈ ilmenite. The boundary between the weathering rind and the surrounding soil matrix material, a feature not previously studied, is marked by an indurated crust, bordered by Fe and Mn enrichment. The rind-crust and crust-soil matrix boundaries are abrupt and elemental concentrations of Mn, Al, Ba, Si, and Mg increase across the crust and matrix indicating enrichment, relative to the weathering rind.

Uranium-series disequilibria in the weathering rind are significant and are the result of mobility characteristics of U-series isotopes during weathering including ^{234}U and ^{238}U isotope fractionation during chemical leaching and the addition of ^{234}U and ^{238}U isotopes into weathering rinds by circulating pore fluids. Uranium-series disequilibria are linked to the rind formation processes of porosity genesis and precipitation of Fe-Al oxides initiated at the core-rind boundary. The U-series disequilibria constrain weathering rind ages which increase with distance from the core-rind boundary to a maximum of ~66 ka in the outer rind, or a mean rind advance rate of ~0.2 mm kyr^{-1}. The rind advance rate calculated here in the Lezarde watershed (MAP = 4500 mm and MAT = 25°) is comparable to the previously measured Bras David (MAP = 3400 mm and MAT = 23°) watershed rind advance rate of 0.18 mm kyr^{-1} (Ma et al., 2012) and ~60% faster than the 0.08 mm kyr^{-1} in the Deshaises (MAP = 1800 mm and MAT = 23 °C) watershed (Engel et al., 2016), independently demonstrating the control of precipitation on weathering rates over a time scale of ~75 kyr. Weathering rinds are thus a suitable system for investigating long-term chemical weathering across environmental gradients.

The synchrotron-source X-ray microprobe was used to examine the distribution and speciation of Fe and Mn in the core and weathered products (rind, crust and matrix material). Iron data indicate a transition from Fe(II)-bearing minerals in the unweathered core to secondary Fe(III)-oxides in the rind. Iron-oxide enrichment around pores in the rind suggests secondary precipitation following the dissolution of primary minerals. Similarly, Mn experiences redox changes in the weathering products, becoming progressively more oxidized from the core to the rind to the matrix. Manganese was present in Fe-rich minerals within the Ca-rich core and but formed distinct Mn-rich crusts along fractures demarcating the crust. Manganese in the crusts was reduced relative to Mn contained in surrounding Fe-rich phases that dominate the weathered rinds, but the specific Mn-bearing mineral phases remain unclear. Although uranium was too dilute in these samples to be resolved using these techniques, information regarding Fe and Mn speciation may indicate mechanisms of U immobilization. For example, Fe and Mn-rich phases that accumulate along pore boundaries and fractures may provide reactive surfaces that sorb U(VI). Alternatively, Mn(II) and/or Fe(II) species may reduce soluble U(VI) to insoluble U(IV).

Acknowledgements

This research was funded by National Science Foundation grants EAR-1251969 to PBS, EAR-1251952 to LM and EAR-1251875 to SLB. SLB acknowledges support for this weathering research from Department of Energy (DOE) grant DE-FG02-05ER15675. MM acknowledges support from a GSA Stephen Pollock Undergraduate Research Grant and the Dickinson College Research and Development Committee. Portions of this work were performed at GeoSoilEnviroCARS (Sector 13), Advanced Photon Source (APS), Argonne National Laboratory. GeoSoilEnviroCARS is supported by the National Science Foundation - Earth Sciences (EAR-1128799) and

Department of Energy- GeoSciences (DE-FG02-94ER14466). This research used resources of the Advanced Photon Source, a U.S. Department of Energy (DOE) Office of Science User Facility operated for the DOE Office of Science by Argonne National Laboratory under Contract No. DE-AC02-06CH11357. Rob Dean (Dickinson College) assisted in the laboratory, J. Engel (UTEP) assisted in the field, and the Observatoire Volcanologique et Sismologique de Guadeloupe (OVSG-IPGP) provided logistical support. C. Dessert is thanked for her help. Constructive reviews by two anonymous reviewers and Editor Michael Boettcher greatly improved this paper.

References

Akob, D.M., Bohu, T., Beyer, A., Schäffner, F., Händel, M., Johnson, C.A., Merten, D., Büchel, G., Totsche, K.U., Küsel, K., 2014. Identification of Mn (II)-oxidizing bacteria from a low-pH contaminated former uranium mine. Appl. Environ. Microbiol. 80 (16), 5086–5097.

Anderson, S.P., Dietrich, W.E., Brimhall, G.H., 2002. Weathering profiles, mass-balance analysis, and rates of solute loss: linkages between weathering and erosion in a small, steep catchment. Geol. Soc. Am. Bull. 114, 1143–1158.

Bargar, J.R., Webb, S.M., Tebo, B.M., 2005. EXAFS, XANES and in-situ SR-XRD characterization of biogenic manganese oxides produced in sea water. Phys. Scr. T115, 888–890.

Barshad, I., 1964. Chemistry of soil development. In: Bear, F.E. (Ed.), Chemistry of the Soil. Reinhold Publishing, New York, pp. 1–70.

Bluth, G.J.S., Kump, L.R., 1994. Lithologic and climatologic controls of river chemistry. Geochim. Cosmochim. Acta 58, 2341–2359.

Brantley, S.L., White, T.S., Ragnarsdottir, K.V., 2007a. The critical zone: where rock meets life. Elements 3, 368.

Brantley, S.L., Godhaber, M.B., Ragnarsdottir, K.V., 2007b. Crossing disciplines and scales to understand the critical zone. Elements 3, 370-314.

Brantley, S.L., Holleran, M.E., Jin, L., Bazilevskaya, E., 2013. Probing deep weathering in the Shale Hills Critical Zone Observatory, Pennsylvania (USA): the hypothesis of nested chemical reaction fronts in the subsurface. Earth Surf. Process. Landf. 28.

Braun, J.J., Descloitres, M., Riotte, J., Fleury, S., Barbiéro, L., Boeglin, J.L., ... Kumar, M.M., 2009. Regolith mass balance inferred from combined mineralogical, geochemical and geophysical studies: mule hole gneissic watershed, South India. Geochim. Cosmochim. Acta 73 (4), 935–961.

Brimhall, G.H., Dietrich, W.E., 1987. Constitutive mass balance relations between chemical composition, volume, density, porosity, and strain in metasomatic hydrochemical systems: results on weathering and pedogenesis. Geochim. Cosmochim. Acta 51, 567–587.

Brimhall, G.H., Chadwick, O.A., Lewis, C.J., Compston, W., Williams, I.S., Danti, K.J., Dietrich, W.E., Power, M.E., Hendricks, D., Bratt, J., 1991. Deformational mass transport and invasive processes in soil evolution. Science 255, 695–702.

Buss, H.L., Sak, P.B., Webb, S.M., Brantley, S.L., 2008. Weathering of the Rio Blanco quartz diorite, Luquillo Mountains, Puerto Rico: coupling oxidation, dissolution and fracturing. Geochim. Cosmochim. Acta 72, 4488–4507.

Calmels, D., Galy, A., Hovius, N., Bickle, M., West, A.J., Chen, M.C., Chapman, H., 2011. Contribution of deep groundwater to the weathering budget in a rapidly eroding mountain belt, Taiwan. Earth Planet. Sci. Lett. 303, 48–58.

Cernohouz, J., Solc, I., 1966. Use of sandstone wanes and weathered basaltic crust in absolute chronology. Nature 212, 806–807 (Nature 387, 491-497).

Chabaux, F., Riotte, J., Dequincey, O., 2003. U-Th-Ra fractionation during weathering and river transport. Rev. Mineral. Geochem. 52, 533–576.

Chadwick, O.A., Derry, L.A., Vitousek, P.M., Huebert, B.J., Hedin, L.O., 1999. Changing Sources of Nutrients during Four Million Years of Ecosystem Development.

Chapnick, S.D., Moore, W.S., Nealson, K.H., 1982. Microbially mediated manganese oxidation in a freshwater lake. Limnol. Oceanogr. 27 (6), 1004–1014.

Chinn, T.J.H., 1981. Use of rock weathering-rind thickness for Holocene absolute age-dating in New Zealand. Arct. Alp. Res. 13, 33–45.

Colman, S.M., 1982a. Clay mineralogy of weathering rinds and possible implications concerning the sources of clay minerals in soil. Geology 10, 370–375.

Colman, S.M., 1982b. Chemical weathering of basalts and basaltic andesites: evidence from weathering rinds. In: U.S.G.S. Professional Paper, (51 p.).

Colman, S.M., Pierce, K.L., 1981. Weathering rinds on andesitic and basaltic stones as a Quaternary age indicator. Western United States. In: U.S.G.S. Professional Paper, (41 p.).

Dessert, C., Lajeunesse, E., Lloret, E., Clergue, C., Crispi, O., Gorge, C., Quidelleur, X., 2015. Controls on chemical weathering on a mountainous volcanic tropical island: Guadeloupe (French West Indies). Geochim. Cosmochim. Acta 171, 216–237.

Dequincey, O., Chabaux, F., Clauer, N., Sigmarsson, O., Liewig, N., Leprun, J.-C., 2002. Chemical mobilizations in laterites: evidence from trace elements and ^{238}U–^{234}U–^{230}Th disequilibria. Geochim. Cosmochim. Acta 66, 1197–1210.

Diem, D., Stumm, W., 1984. Is dissolved manganese being oxidized by O_2 in the absence of Mn bacteria or surface catalysts? Geochim. Cosmochim. Acta 48, 1571–1573.

Drever, J.I., Zobrist, J., 1992. Chemical weathering of silicate rocks as a function of elevation in the southern Swiss Alps. Geochim. Cosmochim. Acta 56, 3209–3216.

Emberson, R., Hovius, N., Galy, A., Marc, O., 2016. Chemical weathering in active mountain belts controlled by stochastic bedrock landsliding. Nat. Geosci. 9, 42–45.

Engel, J.M., Ma, L., Sak, P.B., Gaillardet, J., Minghua, R., Engle, M.A., Brantley, S.L., 2016. Quantifying chemical weathering rates along a precipitation gradient on Basse-Terre Island, French Guadeloupe: New insights from U-series isotopes in weathering rinds. Geochim. Cosmochim. Acta 195, 26–67.

Feldman, C., 1983. Behavior of trace refractory minerals in the lithium metaborate fusion-acid dissolution procedure. Anal. Chem. 55, 2451–2453.

Gaillardet, J., Rad, S., Rive, K., Louvat, P., Gorge, C., Allegre, C.J., Lajeunesse, E., 2011. Orography-driven chemical denudation in the Lesser Antilles: evidence for a new feed-back mechanism stabilizing atmospheric CO_2. Am. J. Sci. 311, 851–894.

Gascoyne, M., 1992. Geochemistry of the actinides and their daughters. In: Ivanovich, M., Harmon, R.S. (Eds.), Uranianium-Series Disequilibrium: Application to Earth, Marine, and Environmental Sciences. Oxford Sciences Publications, Oxford, pp. 34–61.

Ghaleb, B., Hillaire-Marcel, C., Causse, C., Gariepy, C., Vallieres, S., 1990. Fractionation and recycling of U and Th isotopes in a semiarid endoreic depression of central Syria. Geochim. Cosmochim. Acta 54, 1025–1035.

Gislason, S., Eugster, H.P., 1987. Meteoric water–basalt interaction I: a laboratory study. Geochim. Cosmochim. Acta 51, 2827–2840.

Hastings, D., Emerson, S., 1986. Oxidation of manganese by spores of a marine *Bacillus*: kinetic and thermodynamic considerations. Geochim. Cosmochim. Acta 50, 1819–1824.

Hausrath, E.M., Navarre-Sitchler, A., Sak, P.B., Steefel, C.I., Brantley, S.L., 2008. Basalt weathering rates on Earth and the duration of liquid water on the plains of Gusev Crater, Mars. Geology 36, 67–70.

Hilton, R.G., Meunier, P., Hovius, N., Bellingham, P.J., Galy, A., 2011. Landslide impact on organic carbon cycling in a temperate montane forest. Earth Surf. Process. Landf. 36, 1670–1679.

Herndon, E.M., Martinez, C.E., Brantley S, 2014. Spectroscopic (XANES/XRF) characterization of contaminant manganese cycling in a temperate watershed. Biogeochemistry 121, 505–517.

Holbrook, W.S., Riebe, C.S., Elwaseif, M., Hayes, J.L., Basler-Reeder, K., Harry, D.L., Malazian, A., Dosseto, A., Hartsough, P.C., Hopmans, J.W., 2014. Geophysical constraints on deep weathering and water storage potential in the Southern Sierra Critical Zone Observatory: geophysical constraints on weathering in the Southern Sierra CZO. Earth Surf. Process. Landf. 39 (3), 366–380. https://doi.org/10.1002/esp.3502.

Huffman, G.J., et al., 2007. The TRMM multisatellite precipitation analysis (TMPA): quasi-global, multiyear, combined-sensor precipitation estimates at fine scales. J. Hydrometeorol. 8 (1), 38–55.

Ingamells, C.O., 1970. Lithium metaborate flux in silicate analysis. Anal. Chim. Acta 52, 323–334.

Ivarson, K.C., Heringa, P.K., 1972. Oxidation of manganese by microorganisms in manganese deposits of Newfoundland soil. Can. J. Soil Sci. 52 (3), 401–416.

Keiluweit, M., Nico, P., Harmon, M.E., Mao, J., Pett-Ridge, J., Kleber, M., 2015. Long-term litter decomposition controlled by manganese redox cycling. Proc. Nat. Acad. Sci. 112 (38), E5253–E5260.

Kirkbride, M.P., 2005. Boulder edge-roundness as an indicator of relative age: a Lochnagar case study. Scott. Geogr. J. 121, 219–236.

Kirkbride, M.P., Bell, C.M., 2010. Edge-roundness of boulders of Torridonian Sandstone (Northwest Scotland): applications for relative dating and implications for warm and cold climate weathering rates. Boreas 39, 187–198.

Knuepfer, P.L.K., 1988. Estimating ages of late Quaternary stream terraces from analysis of weathering rinds and soils. Geol. Soc. Am. Bull. 100, 1224–1236.

Kraft, S., Stümpel, J., Becker, P., Kuetgens, U., 1996. High resolution x-ray absorption spectroscopy with absolute energy calibration for the determination of absorption edge energies. Rev. Sci. Instrum. 67 (3), 681–687.

Lan, S., Wang, X., Xiang, Q., Yin, H., Tan, W., Qiu, G., Liu, F., Zhang, J., Feng, X., 2017. Mechanisms of Mn (II) catalytic oxidation on ferrihydrite surfaces and the formation of manganese (oxyhydr) oxides. Geochim. Cosmochim. Acta 211, 79–96.

Latham, A.G., Schwarcz, H.P., 1987a. On the possibility of determining rates of removal of uranium from crystalline igneous rocks using U-series disequilibria – 1: a U-leach model, and its applicability to whole-rock data. Appl. Geochem. 2, 55–65.

Latham, A.G., Schwarcz, H.P., 1987b. On the possibility of determining rates of removal of uranium from crystalline igneous rocks using U-series disequilibria – 2: applicability of a U-leach model to mineral separates. Appl. Geochem. 2, 67–71.

Lebedeva, M.I., Fletcher, R.C., Balashov, V.N., Brantley, S.L., 2007. A reactive-diffusion model describing transformation of bedrock to saprolite. Chem. Geol. 244, 624–645.

Lebedeva, M.I., Sak, P.B., Ma, L., Brantley, S.L., 2015. Using a mathematical model of a weathering clast to explore the effects of curvature on weathering. Chem. Geol. 404, 88–99.

Louvat, P., Allegre, C.J., 1997. Present denudation rates on the island of Reunion determined by river geochemistry: basalt weathering and mass budget between chemical and mechanical erosions. Geochim. Cosmochim. Acta 61, 3645–3669.

Ma, L., Wei, J., Xu, G., Long, G., Sun, D., 2007. Mobilization and re-distribution of major and trace elements during extreme weathering of basalt in Hainan Island, South China. Geochim. Cosmochim. Acta 71, 3223–3237.

Ma, L., Chabaux, F., Felt, E., Granet, M., Sak, P.B., Gaillardet, J., Lebedeva, M., Brantley, S.L., 2012. The effect of curvature on the weathering rind formation: evidence from Uranium-series isotopes in basaltic andesite weathering clasts in Guadeloupe. Geochim. Cosmochim. Acta 80, 92–107.

Ma, L., Dosseto, A., Gaillardet, J., Sak, P., Brantley, S., 2018. Quantifying Weathering Rind Formation Rates by In Situ Measurements of U-Series Disequilibria with Laser Ablation (LA) MC-ICPMS. (To be submitted to GCA).

Maher, K., DePaolo, D.J., Lin, J.C.-F., 2004. Rates of silicate dissolution in deep-sea sediment: in situ measurement using 234U/238U of pore fluids. Geochim. Cosmochim. Acta 68, 4629–4648.

Manceau, A., Nagy, K.L., 2012. Quantitative analysis of sulfur functional groups in natural organic matter by XANES spectroscopy. Geochim. Cosmochim. Acta 99, 206–223.

Mann, S., Sparks, N.H.C., Scott, G.H.E., De Vrind-de Jong, E.W., 1988. Oxidation of manganese and formation of Mn_3O_4 (hausmannite) by spore coats of a marine *Bacillus* sp. Appl. Environ. Microbiol. 54, 2140–2143.
Marshall, C.E., 1977. Physical Chemistry and Mineralogy of Soils. Vol. II Wiley and Sons.
Mayanna, S., Peacock, C.L., Schäffner, F., Grawunder, A., Merten, D., Kothe, E., Büchel, G., 2015. Biogenic precipitation of manganese oxides and enrichment of heavy metals at acidic soil pH. Chem. Geol. 402, 6–17.
Meybeck, M., 1987. Global chemical-weathering of surfical rocks estimated from river dissolved loads. Am. J. Sci. 287, 401–428.
Millot, R., Gaillardet, J., Dupré, B., Allègre, C.J., 2002. The global control of silicate weathering rates and the coupling with physical erosion: new insights from rivers of the Canadian Shield. Earth Planet. Sci. Lett. 196 (1), 83–98.
Milnes, A.R., Fitzpatrick, R.W., 1989. Titanium and zirconium minerals. In: Dixon, J.B., Weed, S.B. (Eds.), Minerals and Soil Environments. Book Series No. 1 Vol. SSSA. Soil Science Society of America, pp. 1131–1205.
Morgan, J.J., 2005. Kinetics of reaction between O_2 and Mn(II) species in aqueous solutions. Geochim. Cosmochim. Acta 69 (1), 35–48.
Murray, J.J., Dillard, J.G., Giovanoli, R., Moers, H., Stumm, W., 1985. Oxidation of Mn (II): initial mineralogy, oxidation state and aging. Geochim. Cosmochim. Acta 49, 463–470.
Navarre-Sitchler, A., Brantley, S.L., 2007. Basalt weathering across scales. Earth Planet. Sci. Lett. 261, 321–334.
Navarre-Sitchler, A., Steefel, C., Sak, P.B., Brantley, S.L., 2011. A reactive-transport model for weathering rind formation on basalt. Geochim. Cosmochim. Acta 75, 7644–7667.
Newville, M., 2013. Larch: an analysis package for XAFS and related spectroscopies. In: Journal of Physics: Conference Series. Vol. 430, No. 1. IOP Publishing, pp. 012007.
O'Day, P.A., Rivera, N., Root, R., Carroll, S.A., 2004. X-ray absorption spectroscopic study of Fe reference compounds for the analysis of natural sediments. Am. Mineral. 89 (4), 572–585.
Oguchi, C.T., 2004. A porosity-related diffusion model of weathering-rind development. Catena 58, 65–75.
Parsekian, A.D., Singha, K., Minsley, B.J., Holbrook, W.S., Slater, L., 2015. Multiscale geophysical imaging of the critical zone: geophysical imaging of the critical zone. Rev. Geophys. https://doi.org/10.1002/2014RG000465.
Pelt, E., Chabaux, F., Innocent, C., Navarre-Sitchler, A., Sak, P.B., Brantley, S.L., 2008. Uranium-thorium chronometry of weathering rinds: rock alteration rate and paleo-isotopic record of weathering fluids. Earth Planet. Sci. Lett. 276, 65–75.
Plater, A.J., Ivanovich, M., Dugdale, R.E., 1992. Uranium series disequilibrium in river sediments and waters: the significance of anomalous activity ratios. Appl. Geochem. 7, 101–110.
Post, J.E., 1999. Manganese oxide minerals: Crystal structures and economic and environmental significance. Proc. Natl. Acad. Sci. 96, 3447–3454.
Pouchou, J.L., Pichou, F., 1987. Basic expression of "PAP" computation for quantitative EPMA. In: Brown, J.D., Packwood, R.H. (Eds.), International Congress, 11th X-Ray Optics and Microanalysis. Ontario Univ. Press, pp. 249–252.
Raymond, P.A., 2017. Temperature versus hydrologic controls of chemical weathering fluxes from United States forests. Chem. Geol. 458, 1–13.
Rosholt, J., Doe, B., Tatsumoto, M., 1966. Evolution of the isotopic composition of uranium and thorium in soil profiles. Geol. Soc. Am. Bull. 77, 987–1004.
Sak, P.B., Fisher, D.M., Gardner, T.W., Murphy, K., Brantley, S.L., 2004. Rates of weathering rind formation on Costa Rican basalt. Geochim. Cosmochim. Acta 68, 1453–1472.
Sak, P.B., Navarre-Sitchler, A., Miller, C.E., Daniel, C.C., Gaillardet, J., Buss, H.L., Lebedeva, M.I., Brantley, S.L., 2010. Controls on rind thickness on basaltic andesite clasts weathering in Guadeloupe. Chem. Geol. 276, 129–143.
Samper, A., Quidelleur, X., Lahitte, P., Mollex, D., 2007. Timing of effusive volcanism and collapse events within an oceanic arc island: Basse-Terre, Guadeloupe archipelago (Lesser Antilles Arc). Earth Planet. Sci. Lett. 258, 175–191.
Santelli, C.M., Pfister, D.H., Lazarus, D., Sun, L., Burgos, W.D., Hansel, C.M., 2010. Promotion of Mn(II) oxidation and remediation of coal mine drainage in passive treatment systems by diverse fungal and bacterial communities. Appl. Environ. Microbiol. 76, 4871–4875.
Santelli, C.M., Webb, S.M., Dohnalkova, A.C., Hansel, C.M., 2011. Diversity of Mn oxides produced by Mn(II)-oxidizing fungi. Geochim. Cosmochim. Acta 75, 2762–2776.
Schaefer, M.V., Handler, R.M., Scherer, M.M., 2017. Fe(II) reduction of pyrolusite (β-Mn02) and secondary mineral evolution. Geochem. Trans. 18, 7. https://doi.org/10.1186/s12932-017-0045-0.
Sims, K.W.W., Gill, J.B., Dosseto, A., Hoffmann, D.L., Lundstrom, C.C., Williams, R.W., Ball, L., Tollstrup, D., Turner, S., Prytulak, J., Glessner, J.G., Standish, J.J., Elliott, T., 2008. An inter-laboratory assessment of the thorium isotopic composition of synthetic and rock reference materials. Geostand. Geoanal. Res. 32, 65–91.
Stefansson, A., Gislason, S.R., 2001. Chemical weathienrg of basalts, southwest Iceland: effect of rock crystallinity and secondary minerals on chemical fluxes to the ocean. Am. J. Sci. 301, 513–556.
Stumm, W., Morgan, J.J., 1996. Aquatic chemistry: chemical equilibria and rates in natural waters. Wiley, New York.
Suhr, N.H., Ingamells, C.O., 1966. Solution technique for analysis of silicates. Anal. Chem. 38, 730–734.
Tebo, B.M., Bargar, J.R., Clement, B.G., Dick, G.J., Murray, K.J., Parker, D., Verity, R., Webb, S.M., 2004. Biogenic manganese oxides: Properties and mechanisms of formation. Annu. Rev. Earth Planet. Sci. 32, 287–328.
Tebo, B.M., Johnson, H.A., McCarthy, J.K., Templeton, A.S., 2005. Geomicrobiology of manganese (II) oxidation. Trends Microbiol. 13, 421–428.
Vigier, N., Bourdon, B., Turner, S., Allegre, C.J., 2001. Erosion timescales derived from U-decay series measurements in rivers. Earth Planet. Sci. Lett. 193, 485–499.
Villalobos, M., Lanson, B., Manceau, A., Toner, B., Sposito, G., 2006. Structural model for the biogenic Mn oxide produced by *Pseudomonas putida*. Am. Mineral. 91, 489–502.
Walker, J., Hays, P., Kasting, J., 1981. A negative feedback mechanism for the long-term stabilization of Earth's surface temperature. J. Geophys. Res. 86, 9776–9782.
Wang, X., Lan, S., Zhu, M., Ginder-Vogel, M., Yin, H., Liu, F., Tan, W., Feng, X., 2015. The presence of ferrihydrite promotes abiotic formation of manganese (oxyhydr)oxides. Soil Sci. Soc. Am. J. 79 (5), 1297–1305.
Webb, S.M., Dick, G.J., Bargar, J.R., Tebo, B.M., 2005. Evidence for the presence of Mn (III) intermediates in the bacterial oxidation of Mn(II). Proc. Natl. Acad. Sci. 102, 5558–5563.
West, A.J., Galy, A., Bickle, M.J., 2005. Tectonic and climatic controls on silicate weathering. Earth Planet. Sci. Lett. 235, 211–228.
White, A.F., 1995. Chemical weathering rates of silicate minerals in soils. In: White, A.F., Brantley, S.L. (Eds.), Chemical Weathering Rates of Silicate Minerals. Rev. Mineral. 31. Mineralogical Society of America, pp. 407–461.
White, A.F., Blum, A.E., Schultz, M.S., Vivit, D.V., Stonestrom, D.A., Larsen, M., Murphy, S.F., Eberl, D., 1998. Chemical weathering in a tropical watershed, Luquillo Mountains, Puerto Rico: long-term versus short-term weathering fluxes. Geochim. Cosmochim. Acta 62, 209–226.
White, A.F., Bullen, T.D., Schultz, M.S., Blum, A.E., Huntington, T.G., Peters, N.E., 2001. Differential rates of feldspar weathering in grantic regoliths. Geochim. Cosmochim. Acta 65, 847–869.
Whitehouse, I.E., McSaveney, M.J., Knuepfer, P.L.K., Chinn, T.J.H., 1986. Growth of weathering rinds on Torlesse Sandstone, Southern Alps, New Zealand. In: Rates of Chemical Weathering of Rocks and Minerals. Academic Press, pp. 419–435.
Yoshida, H., Metcalfe, R., Nishimoto, S., Yamamoto, H., Katsuta, N., 2011. Weathering rind formation in buried terrace cobbles during periods of up to 300 ka. Appl. Geochem. 26, 1706–1721.